Supplementary Information (SI) for Energy & Environmental Science.

Electronic supplementary information for

Rapid electrothermal rejuvenation of spent lithium cobalt oxide cathode

Yi Cheng, Jinhang Chen, Weiyin Chen, Qiming Liu, Obinna E. Onah, Zicheng Wang, Gang Wu, Tianyou Xie, Lucas Eddy, Boris I. Yakobson, Ju Li, Yufeng Zhao, and James M. Tour

Experimental section

Materials: The spent LCO cathode was obtained from used commercial 18650-cylinder cells (LGDAHB21865-P308K034A3) from a local recycler in Houston, Texas. The residual capacity of s-LCO was ~90 mAh g^{-1} at 0.2 C in the cycling potential range of 3.0-4.2 V (Fig. S53, ESI†). The spent NMC (s-NMC) 111 cathode was harvested from a commercial pouch cell (AA Portable Power Corp.), which was cycled between 2.8 – 4.3 V with a charge/discharge current of 1000 mA (0.5 C) for 200 cycles, and discharged to 2.0 V. The cell presented 75% of the initial capacity after cycling. The as-received spent cathode powders were calcined in a muffle furnace (Carbolite RHF 1500) at 600 °C in the air for 2 h to remove the polymer binder and carbon. The chemicals used include MgO (Sigma Aldrich, 99%), Al_2O_3 (Sigma Aldrich, 99%,), TiO_2 (Sigma Aldrich, 97%), and MnO_2 (Sigma Aldrich, 90%). The commercial LCO used as the comparison is purchased from Sigma Aldrich (99.8% trace metals basis). The carbon felt (PAN-6.3 mm thick) and carbon paper (Toray Carbon Paper 060) were purchased from the Fuel Cell Store. For the battery assembly, polyvinylidene fluoride binder (PVDF, MTI Corporation) and high-conductivity acetylene black (ABHC-01, Soltex Corporation) were used to prepare the battery slurry. The electrolyte was 1 M $LiPF_6$ (battery grade, Millipore-Sigma) dissolved in ethylene carbonate (EC) and ethyl methyl carbonate (EMC) with a volume ratio of 3:7. Lithium chips (D = 16 mm, t = 0.6 mm, 99.9%, MTI Corporation) were served as the counter electrode in the half cell. Graphite powder (MesoCarbon MicroBeads, MTI Corporation) was used to prepare the anode for the full cell.

Electrothermal cathode upcycling: The spent LCO powders were mixed and hand-milled with 15 wt% Li_2CO_3, and additional MgO and Al_2O_3 as the dopants. The Mg and Al doping concentrations were measured by ICP-MS after the electrothermal treatment, which is listed in Table S4 (ESI†). Carbon felt was used for the heater with a size of ~4.0 cm × 8.0 cm × 6.3 mm. The center of the heater was manually excavated to create a concave area of ~2.4 cm × 4.8 cm × 3.0 mm, where ~500 mg of mixture powder was loaded per batch, and a carbon paper (size of ~2.5 cm × 4.9 cm × 0.19 mm) was further capped on its surface. During the electrothermal process, the carbon heater is connected to a commercial arc welder (DEKOPRO, 110/220 V) as the power source. The heating temperature was measured using an infrared thermometer (Micro-Epsilon, CTM-3SF75H2-C3) with a detecting range of 200-1500 °C. The heating temperature can be modulated by changing the input current from 10 to 60 A (Fig. 1d). Each temperature with a different current input was repeated in 3 parallel experiments. The current profile was measured by a Hall effect sensor (Tamura L34S1T2D15) through a custom LabVIEW program. The energy consumption during the electrothermal process was measured by a power meter (Atorch AC Wattmeter, Amazon). The optimized heating parameters for cathode upcycling is 12 A current input in the air with a stable heating time of 30 s.

Electrochemical tests: The resynthesized LCO cathode, conductive carbon black, and poly(vinyl difluoride) (PVDF) were mixed and ground with a mass ratio of 8:1:1, while *N*-methyl-2-pyrrolidone (NMP) with ~2.5 times of the total mass was added to prepare a homogeneous slurry. The slurry was coated onto an 18-μm-thick carbon-coated aluminum (Al/C) foil by a doctor blade with blade spacing of 250 μm, and dried by a built-in heating cover at 70 °C for 2 h, followed by drying in a vacuum oven at 70 °C under vacuum (~10 mm Hg) overnight. The cathode area was ~1.54 cm^2, and the average loading mass of the active materials was ~7.5 mg. The coin cells (CR2032) were assembled in an argon-filled glove box with moisture and oxygen concentrations below 0.5 ppm. Lithium chips were used as the counter electrode with a polypropylene separator with Al_2O_3 coating (~26 μm, SH416W14, SENIOR INC.). 1 M $LiPF_6$ salt in a mixture of EC and EMC (3:7 vol%) was used as the electrolyte with 50 μL for each cell. All cells were cycled at 0.1 C for 10 cycles before cycling at 0.2 C for stability tests.

For the full cell, commercial graphite (EQ-Lib-MCMB, MTI Corporation) was used as the anode. The graphite powder was mixed and milled with carbon black and PVDF with a mass ratio of 90:5:5 using NMP as the solvent. The mixture was coated on the 8-μm-thick copper foil, and then dried following the same procedures. To mitigate the formation of lithium dendrites during cycling, the capacity of the graphite anode was set in excess when compared to the LCO cathode, with an N/P ratio of ~1.1:1. The calculation was based on equation (1).

$$\frac{C_{anode} \times m_{anode}}{C_{cathode} \times m_{cathode}} = 1.1:1 \tag{1}$$

where C is the specific mass capacity, m is the loading mass. Considering the $C_{cathode}$ is 200 mAh g^{-1} for r-LCO-MA, and C_{anode} is 340 mAh g^{-1} for graphite, graphite loading on the copper foil is set at ~4.8 mg. All full cells were cycled at 0.1 C for 10 cycles before cycling at 0.2 C for stability tests.

CV voltammograms were taken with different scan rates from 0.1 mV s^{-1} to 1 mV s^{-1} in the range of 3.0–4.6 V using a CHI 680D electrochemical workstation. EIS measurements were conducted on the CHI 680D electrochemical workstation by applying an alternating voltage of 5 mV over a frequency ranging from 0.1 Hz to 1 MHz.

For the GITT tests, each coin cell was tested using a battery testing station (CT2001A, LANHE Corporation, China) at 0.2 C, where the duration time of each current pulse (τ) is set as 1800 s with a relaxation time of 7200 s after each pulse.

Characterization: XRD was performed by the Rigaku SmartLab system with filtered Cu Kα radiation (λ = 1.5406 Å). The acquired XRD data were refined and analyzed using GSAS-II software to determine the lattice parameters and chemical compositions of the samples. Temperature-dependent XRD was conducted in the temperature range from 25 to 850 °C. The *in-situ* cathode structure evolution during the electrochemical cycling test was carried out using a PANalytical Empyrean precision powder diffractometer. The homemade 2016-coin cell case with a 10 mm polyimide window was used for the characterization. The XRD system was equipped with a molybdenum X-ray source with a wavelength of 0.7107 Å. The EC coin stage was used to load the coin cell, which was tested at 0.1 C with a voltage range from 3.0 to 4.6 V. Continuous measurements were performed with each measurement from 5 to 30 degrees. Each measuring cycle was ~30 min. Raman spectra were acquired using a Renishaw Raman inVia microscope system (laser wavelength of 532 nm, laser power of 5 mW, 50 × lens). XPS spectra were taken by the PHI Quantera XPS system under a pressure of 5×10^{-9} Torr. The survey spectra were collected with steps of 0.5 eV and pass energy of 140 eV. Elemental XPS spectra were collected at a step size of 0.1 eV and pass energy of 26 eV. All XPS spectra were calibrated using the C 1*s* peak at 284.8 eV as the reference. XPS depth analysis was performed using a 3 keV argon ion beam with an etching area of 3 mm × 3 mm. TGA was conducted on the Mettler Toledo TGA/DSC 3+ system at a heating rate of 10 °C min^{-1} with an airflow rate of 100 $mL\cdot min^{-1}$. SEM images were taken on the FEI Quanta 400 ESEM FEG system at a voltage of 20 kV with a working distance of 10 mm. EDS spectra and maps were obtained through an EDS detector on the system. The HRTEM images were obtained on a JEOL 2100 field emission gun TEM at 200 kV. X-band electron paramagnetic resonance (EPR) spectra were recorded by a Bruker EMX spectrometer (Billerica, MA). The EPR spectra were obtained at a temperature of 295 K in a capillary tube at a frequency of 9.32 GHz, microwave power of 1 mW, modulation frequency of 100 kHz, modulation amplitude of 1.0 G, and time constant of 0.17 s. The element contents of cathode materials were tested by ICP-MS using a Perkin Elmer Nexion 300 ICP-MS system. The standard solutions include: Li, Co, Mg, and Al (1000 mg L^{-1}, 10 wt% HNO_3, Millipore-Sigma). Each element concentration was calculated from 3 parallel ICP tests. Before the test, 10 mg of the sample was digested by 5.0 mL *aqua regia* at 100 °C for 12 h. *Aqua regia* was prepared by mixing nitric acid (67–70 wt%, TraceMetal^{TM} Grade, Fisher Chemical) and hydrochloric acid (37 wt%, 99.99% trace metals basis, MilliporeSigma) at a molar ratio of ~1:3. The digested solution was filtered by a polyether sulfone (PES) membrane (0.22 μm) and then diluted to a range within the calibration curve (1-100 ppb) using ultrapure water (MilliporeSigm, ACS reagent for ultratrace analysis).

Computational Methods: DFT method,[1] as implemented in the Vienna Ab-initio Simulation Package (VASP),[2] was used to study the electronic properties and structural stability of pristine $LiCoO_2$, Mg/Al-doped $LiCoO_2$, and Li_xCoO_2 ($x < 1$). A plane wave expansion to 520 eV was employed, combined with an all-electron-like projector augmented wave (PAW) potential.[3] Exchange correlation was treated within the generalized gradient approximation (GGA) using the functional parameterized by Perdew-Burke-Ernserhof.[4] For the doped structures, 4 × 4 supercells were constructed, and periodic boundary conditions were applied to the supercell in all three dimensions. Based on the size of the unit cell, the convergence of total energy was achieved with respect to k-point sampling for Brillouin zone integration using a Monkhorst-Pack type mesh.[5] In structure optimization, the conjugate-gradient algorithm implemented in VASP was used. Both the atomic positions and unit cells are fully relaxed until the maximum force on each atom is less than 0.01 eV $Å^{-1}$.

The optimized structures were then used as input for molecular dynamic (MD) simulations to test structural stability. All MD modeling tasks were performed using a Nosé-Hoover thermostat and an NVT ensemble at 2250 K for 100 ps. The evolution of the average coordination number of Co atoms (with the Co-O distance cutoff at 2.2 Å) was used as the descriptor of structural transformation. The final Co coordination number for each doping condition was calculated from the average value in the time scale of 60 - 90 ps. To overcome the inaccuracy of DFT calculation in the electronic properties of crystals, the hybridized functional method has to be applied.[6] Here, we chose the Heyd-Scuseria-Ernzerhof screened hybrid functional (HSE06)[7] as implemented in VASP.

Note S1. Sample heating during the RER process.

1.1 Heating temperature control

During RER process, regenerated cathode performance mostly depends on steady heating temperature. When using carbon felt as the sample holder and heating media, with a constant current input (*I*) from an arc welder, the surface temperature of carbon felt increases to a steady temperature within seconds, while the electrothermal input energy (Q_{in}) and heat dissipation to surroundings (Q_{dis}) achieve the balance. The balance can be described as:[8,9]

$$mC_f\frac{dT}{dt} = Q_{in} - Q_{dis} \tag{S1}$$

Where m and C_f are the mass and the heat capacity of the carbon felt, respectively.

The electrothermal input energy, Q_{in}, can be calculated by Equation (S2),

$$Q_{in} = I^2Rt \tag{S2}$$

where I is the current passing through the sample, R is the resistance of carbon felt, and t is the discharging time. For a specific cuboid-shaped carbon felt, its length and width were denoted as a and b, while its thickness (c) was 6.3 mm in the surroundings and ~3.0 mm in the center concave part. R can be further calculated by Equation (S3),

$$R = \rho_{\mathrm{e}}\frac{a}{bc} \tag{S3}$$

where ρ_{e} is the electrical resistivity. The electrical resistivity (ρ_{e}) is constant for a specific sample like carbon felt.

The dissipating heat, Q_{dis}, which comes from the heat conduction from the heated carbon felt to the environment, can be depicted as:

$$Q_{dis} = hab(T_S - T_r)t \tag{S4}$$

where T_{s} is the steady temperature, T_{r} is the room temperature, and h is a heat-transfer coefficient, which is a constant value for a specific sample.

At a steady temperature, the system heat flux reaches a steady state where the electrothermal input energy equals the energy transfer out of the system.

$$Q_{in} = Q_{dis} = hab(T_S - T_r)t \tag{S5}$$

Substituting Equations (S2) and (S3) into Equation (S5), T_{s} can be calculated by reformulated Equation (S6):

$$T_s = I^2\frac{\rho_{\mathrm{e}}}{hb^2c} + T_r \tag{S6}$$

As the theoretical calculation, T_s has a linear relationship with $1/c$, $1/b^2$, and I^2. For the concave carbon felt design, the thickness of the concave area is ~3.0 mm, which is nearly half of its surrounding part (~6.3 mm). Thus, the temperature in the center of the carbon felt is higher than that in the surroundings (Fig. S1c, ESI†), indicating a localized heat for sample heating with a higher energy efficiency.

Based on Equation S6, the heating temperature is related to the felt width (b) and input current (I), but has a negligible relationship with the felt length (a), which is consistent with our experimental temperature results in Fig. S6 (ESI†). Thus, the electrothermal temperature can be precisely modulated from 700 to 1200 °C by changing the width of carbon felt or tuning input current (Fig. 1d and Fig. S6, ESI†).

1.2 Sample heating rate

The sample heating from the carbon felt heater is based on heat conduction, which follows Fourier's law. We assumed that the felt heater first increases to a steady temperature (T_{heater}) and the sample precursors were then uniformly heated to a temperature of T_{sample}. The temperature gradient ($\varDelta T$) was defined as:

$$\varDelta T = T_{\text{heater}} - T_{\text{sample}} \tag{S7}$$

Then, we defined $t = 0$ as the moment when heater temperature is stable but sample kept at room temperature (T_r).

$$\varDelta T_0 = T_{\text{heater}} - T_{\text{sample,0}} = T_{\text{heater}} - T_{\text{r}} \tag{S8}$$

According to the instantaneous heat transfer, the relationship between T_{sample} and the time (t) can be expressed as:

$$t = \frac{\rho_s V_s C_s}{h A_s} \ln \frac{\varDelta T_0}{\varDelta T} \tag{S9}$$

where ρ_s is the density of the sample, V_s is the volume of the sample, C_s is the specific heat capacity of the sample, h is the heat transfer coefficient, and A_s is the heat transfer area between the carbon felt heater and the sample.

Here, V_s is related to A_s and sample loading thickness (d_s),

$$V_s = A_s \times d_s \tag{S10}$$

Thus, Equation (S9) can be simplified as:

$$t = \frac{\rho_s d_s C_s}{h} \ln \frac{\Delta T_0}{\Delta T} \qquad (S11)$$

In our RER process, when the temperature reaches to 90% of steady heating temperature (~750 °C), the cation insertion into LCO can be triggered (Fig. 1b and Figs. S2-S4, ESI†). Here, we defined t_{90} as the time required to heat the sample to 90% of the carbon felt heater temperature ($T_{\mathrm{sample}} = 0.90 T_{\mathrm{heater}}$).

$$t_{90} = \frac{\rho_s d_s C_s}{h} \ln \frac{T_{\mathrm{heater}} - T_{\mathrm{r}}}{0.1 T_{\mathrm{heater}}} \qquad (S12)$$

Where t_{90} is only related to d_s. Therefore, once sample loading thickness is same, we can enlarge our RER system by increase the felt heater width and length while keeping the time required to sample heating constant.

Note S2. Galvanostatic intermittent titration technique for Li^+ diffusion test.

The Li^+ diffusion coefficients of different LCO samples (D_{Li+}) were measured by the galvanostatic intermittent titration technique (GITT). Based on Fick's second law, the Li^+ diffusivity can be quantified by measuring the potential variation with the state-of-charge (SOC). During the tests, the GITT curve was tested with the cycling rate of 0.2 C, where the duration time of each current pulse (τ) is set as 1800 s with a relaxation time of 7200 s after each pulse. The voltage is recorded every 10 s (Figs. S41 and S42, ESI†).

During the charging process, the initial rapid potential increase can be attributed to the electrical internal resistance of the electrodes. Afterwards, the potential increase is ascribed to the electrochemical Li^+ deintercalation during the galvanostatic charging. After each current pulse, the potential instantaneously decreases due to the electrical internal resistance. Finally, it gradually reaches the quasi-equilibrium open circuit potential.[10,11]

Then the $D_{Li}{}^+$ could be calculated as Equation (S13):

$$D_{\mathrm{Li+}} = \frac{4}{\pi\tau}\left(\frac{n_B V_B}{S}\right)^2 \left(\frac{\Delta E_s}{\Delta E_\tau}\right)^2 \qquad (S13)$$

where $D_{Li}{}^+$ ($cm^2\ s^{-1}$) is the chemical diffusion coefficient of Li^+; τ is the duration of the current pulse (s, $\tau = 1800$ s). n_B is the moles (mol) of active material, V_B ($cm^3\ mol^{-1}$) is molar volume; S (cm^2) is the apparent area of electrode area; τ (s) is the pulse time; ΔE_τ (V) is the potential change in a single-step of the current pulse; ΔE_s (V) is the steady-state potential change between steps.

Note S3. Calculation the ratio of unoccupied O 2p orbitals and their average energy in $Li_{0.2}CoO_2$.

To evaluate the structural stability of $Li_{0.2}CoO_2$ before and after Mg/Al doping, we calculated electron state ratios in unoccupied orbitals (*r(unoccupied)*) and average electron energy of unoccupied orbitals ($\bar{E}(unoccupied)$) based on the simulated projected density of state (DOS) of O 2p.

Firstly, *r(unoccupied)* was calculated according to Equation (S14):

$$r(unoccupied) = \frac{S(unoccupied)}{S(total)} = \frac{\int_{E_F}^{+\infty} SdE}{\int_{-\infty}^{+\infty} SdE} \qquad (S14)$$

Here, *S(unoccupied)* and *S(total)* are electron states in unoccupied orbitals and total orbitals. S (unit: states eV^{-1}) represents the electron states under specific energy (E, unit: eV).

r(unoccupied) for bare $Li_{0.2}CoO_2$ is calculated to be 15.0%. In comparison, this value drops to 14.4% after Mg/Al doping, indicating less unoccupied O 2p orbitals after doping.

The average electron energy of unoccupied orbitals ($\bar{E}(unoccupied)$) is calculated based on Equation (S15):

$$\bar{E}(unoccupied) = \frac{\int_{E_F}^{+\infty} SEdE}{\int_{E_F}^{+\infty} SdE} \qquad (S15)$$

Where E_F is normalized to 0.

$\bar{E}(unoccupied)$ for bare $Li_{0.2}CoO_2$ is calculated to be 0.53 eV, while $\bar{E}(unoccupied)$ decreases to 0.47 eV after Mg/Al doping, indicating lower reaction probability for the oxygen atoms in LCO lattice after doping.

Note S4. Electrical energy consumption.

The energy consumption of the electrothermal upcycling process is calculated using Equation (S16),

$$E = \frac{E_0}{M} \tag{S16}$$

Where E is the consumed energy per gram (kJ g^{-1}), E_0 is the measured energy consumption by an electric meter, and M is the mass of regenerated cathode per batch.

During the electrothermal regeneration process, with E_0 = 2.8 kJ and M = 0.46 g, the power consumption is calculated to be: E = 5.6 kJ g^{-1} = 1.69 kWh kg^{-1}.

Given that the industrial price of electrical energy in Texas, USA is \$0.0644 kWh, the energy cost for 1 kg of cathode regeneration can be estimated to be: P = \$0.109 kg^{-1}.

Note S5. Life cycle analysis and techno-economic assessment.

5.1 Goal and scope.

The closed-loop life cycle analysis aims to compare the potential economic and environmental effects of different cathode waste recycling processes, including the pyrometallurgical method, the hydrometallurgical method, the direct recycling method, and the RER method in this work. Specifically, energy consumption, GHG emission, and water consumption are analyzed following the ISO 14044 requirements.[12]

5.2 Scenario description and system boundaries.

Four scenarios were considered in this study (Fig. S52, ESI†). In each scenario, 1 kg of spent lithium-ion batteries were used as the baseline for the cathode recycling. All material and energy flows are normalized to treating 1 kg of spent lithium-ion batteries (Table S5, ESI†).

Scenario 1 Pyrometallurgical method: In this scenario,[13,14] 1 kg of spent lithium-ion batteries were disassembled and smelted after discharging. The smelting process was then conducted to decompose the binders, electrolytes and cathode electrolyte interphase (CEI) impurities, and thermally reduce the cathode materials into their metal counterparts (0.39 kg). In the following acid-leaching process, the amount of acid was set based on the mass of the solid and the pulp density (~5%), and the HCl concentration was 1 mol L^{-1}. Note that we assume that ~95% HCl can be reused after leaching. Subsequently, 0.34 kg of metal hydroxide was mixed with lithium carbonate (0.15 kg) and then regenerated by furnace heating. Finally, 0.36 kg of regenerated LCO cathode can be obtained.

Scenario 2 Hydrometallurgical method: In this scenario,[14] 1 kg of spent lithium-ion batteries were disassembled, crushed, and shredded after discharging. The collected battery pieces (0.88 kg) were calcined to decompose the binders, electrolytes, and CEI impurities. The following wet granulation, density separation, and froth flotation were applied to separate cathode materials (0.35 kg) from other battery parts. Afterwards, the acid was added to leach the Li and Co elements from the waste cathode, where the acid amount was calculated based on the mass of the solid and the pulp density (~2%), and the HCl concentration was set as 4 mol L^{-1}. Note that we assume that ~95% HCl can be reused after leaching. Subsequently, the metal ions were precipitated under nitrogen with a pH value of 10-11. After filtration and drying, 0.33 kg of LiOH and $Co(OH)_2$ can be obtained. The precipitates (0.33 kg) were mixed with lithium carbonate (0.14 kg) and then regenerated by furnace heating. Finally, 0.35 kg of regenerated LCO cathode can be obtained.

Scenario 3 Direct recycling: In this scenario,[15,16] 1 kg of spent batteries were shredded to collect the spent cathode waste after discharging. NMP solvents (3.70 kg) were used to wash the collected cathode material to remove the polymer binder. After filtration, ~95% NMP solvent can be reused for further cathode washing, and 0.37 kg of separated cathode materials were calcined to remove the impurities. The purified cathode was mixed with 15 wt% Li_2CO_3 (0.05 kg), and then calcined in the furnace for the lithiation. Finally, 0.37 kg of regenerated LCO cathode can be obtained.

Scenario 4 RER: In this scenario, 1 kg of spent batteries were shredded to collect the spent cathode waste after discharging. After separation, 0.37 kg of cathode materials were calcined to remove the impurities. The purified cathode (0.35 kg) was mixed with 15 wt% Li_2CO_3 (0.05 kg), 2 wt% MgO (0.007 kg), and 1 wt% Al_2O_3 (0.0035 kg), and then electric heated for the lithiation. Finally, 0.38 kg of regenerated high-voltage LCO cathode can be obtained.

5.3 Life cycle inventory.

The environmental impacts, including energy demand, GHG emission, and water consumption, for the materials production and processing are summarized in Table S6 (ESI†). The values are explained below. Note that 1 MJ of electricity produces 0.13 kg GHG and consumes 0.67 kg water from the Argonne GREET model.[17]

Materials production: The energy consumption, GHG emission, and water consumption for NMP (89.58 MJ kg^{-1}, 5.55 kg kg^{-1}, 3.51 kg kg^{-1}), hydrochloride acid (2.10 MJ kg^{-1}, 29.17 kg kg^{-1}, 4.71 kg kg^{-1}), NaOH (31.96 MJ kg^{-1}, 2.32 kg kg^{-1}, 12.54 kg kg^{-1}), Na_2CO_3 (5.36 MJ kg^{-1}, 0.68 kg kg^{-1}, 0.12 kg kg^{-1}), MgO (12.00 MJ kg^{-1}, 0.90 kg kg^{-1}, 0.27 kg kg^{-1}), Al_2O_3 (11.18 MJ kg^{-1}, 1.00 kg kg^{-1}, 7.99 kg kg^{-1}), and Li_2CO_3 (121.98 MJ kg^{-1}, 12.05 kg kg^{-1}, 44.92 kg kg^{-1}) from the Argonne GREET model[17].

Processing-Discharging and collection: The spent LIBs need to be discharged and disassembled. The cathode and anode materials were collected after removing the case and separator. During this process, the estimated energy consumption was 0.41 MJ kg^{-1}, while the GHG emission and water consumption were 0.054 kg kg^{-1} and 0.78 kg kg^{-1}, respectively, from the Everbatt 2020 database[18].

Processing-Calcination and granulation: The battery materials need to be calcined in the furnace to remove at 873 K for 2 h to remove impurities and granulated to collect cathode materials. During this process, the estimated energy consumption was 0.21 MJ kg^{-1}, while the GHG emission and water consumption were 0.33 kg kg^{-1} and 0.53 kg kg^{-1}, respectively, from the Everbatt 2020 database[18].

Processing-Cathode separation: During this process, the cathode materials were scraped from the aluminum foil. The estimated energy consumption was 0.38 MJ kg^{-1}, while the GHG emission and water consumption were 0.05 kg kg^{-1} and 0.26 kg kg^{-1}, respectively, from the Everbatt 2020 database[18].

Processing-NMP washing: During this process, the scraped cathode was washed by NMP (×20) for 6 h. The estimated energy consumption was 0.78 MJ kg^{-1} from the Everbatt 2020 database. Correspondingly, 0.10 kg kg^{-1} GHG was emitted, and 0.52 kg kg^{-1} water was consumed during this process[18].

Processing-Smelting: The smelting process was applied at 1873 K for 3 h in a furnace. The estimated energy consumption was 2.24 MJ kg^{-1}, while the GHG emission and water consumption were 1.40 kg kg^{-1} and 1.51 kg kg^{-1}, respectively, from the Everbatt 2020 database.[18]

Processing-Low-temperature heating: The scraped cathode materials were put into a furnace and calcined at 873 K for 2 h to decompose the impurities. During this process, the estimated energy consumption was 0.20 MJ kg^{-1}, while the GHG emission and water consumption were 0.526 kg kg^{-1} and 0.14 kg kg^{-1}, respectively, from the Everbatt 2020 database.[18]

Processing-Acid leaching: The pretreated cathode materials were leached by the HCl acid. The estimated energy consumption was 0.11 MJ kg^{-1}, while the GHG emission was 0.014 kg kg^{-1}. Considering the different acid concentrations needed in pyrometallurgical and hydrometallurgical processes, concentrated HCl (12 M) consumptions are 0.69 and 6.33 kg kg^{-1}, respectively, for these two processes. Correspondingly, water consumption is 17.31 and 30.99 kg kg^{-1}. Note when calculating the energy consumption and GHG emissions, we assume that ~95% HCl can be reused after leaching. All data here are from the Everbatt 2020 database.[18]

Processing-Chemical precipitation: The leached metal ions were precipitated by adding some alkali to modulate the pH value. The estimated energy consumption was 0.11 MJ kg^{-1}, while the GHG emission and water consumption were 0.014 kg kg^{-1} and 0.036 kg kg^{-1}, respectively, from the Everbatt 2020 database.[18]

Processing-Cathode resynthesis heating: During this process, the mixture of precipitated metal hydroxide and lithium salts was calcined at 723 K for 5 h and 1173 K for 14 h. The estimated energy consumption was 18.84 MJ kg^{-1}, while the GHG emission and water consumption were 2.95 kg kg^{-1} and 12.63 kg kg^{-1}, respectively, from the Everbatt 2020 database.[18]

Processing-Direct regeneration heating: During this process, the mixture of purified cathode materials and lithium salts was calcined at 1073 K for 12 h. The estimated energy consumption was 7.05 MJ kg^{-1}, while the GHG emission and water consumption were 1.01 kg kg^{-1} and 4.73 kg kg^{-1}, respectively, from the Everbatt 2020 database.[18]

Processing-Electrothermal heating: The energy consumption for electrothermal heating is estimated to be 5.61 MJ kg^{-1}, according to the detailed analysis in Note S3. Correspondingly, 0.82 kg kg^{-1} GHG was emitted, and 3.76 kg kg^{-1} water was consumed during this process.

5.4 Life cycle impact assessment.

In this study, the environmental impacts were classified into three midpoint indicators, including cumulative energy demand (Table S7, ESI†), GHG emission (Table S8, ESI†), and water consumption (Table S9, ESI†).

5.5 Cost and profit evaluation

In this study, the costs for raw materials are from the prices of commercial products, including industrial water (\$1.085 per tonne[19]), NMP (\$2800 per tonne[20]) 12 M HCl (\$179 per tonne[21]), NaOH (\$1315 per kg[22]), Na_2CO_3 (\$284 per tonne[23]), MgO (\$425 per tonne[24]), Al_2O_3 (\$540 per tonne[25]), and Li_2CO_3 (\$15490 per tonne[26]). The costs for energy consumption are calculated according to the industrial electricity rate in Texas, US (\$0.0644 kWh^{-1}, US Energy Information Administration[27]). The values are listed in Table S10 (ESI†).

Next, we calculated the capital cost. 0.88 tonne of dissembled battery pieces from 1.0 tonnes of spent battery needs to be ground by a grinder before further pyrometallurgical, or hydrometallurgical treatment. The price of a grinder is estimated to be \$1000 with an estimated annual treating capacity of 10 tonnes and a lifespan of 20 years[28]. Thus, the capital cost in this process was calculated to be \$4.4 $tonne^{-1}$, when normalized by recycling 1 tonne of spent battery.

Cathode materials from 1 tonne of spent battery need to be scraped from the current collector (0.88 tonne) by a scraper before direct recycling and RER. The price of a scraper is estimated to be \$3000 with an estimated annual treating capacity of 10 tonnes and a lifespan of 20 years[29]. Thus, the capital cost in this process was calculated to be \$13.2 $tonne^{-1}$, when normalized by recycling 1 tonne of spent battery.

In the acid leaching, co-precipitation, and NMP washing process, the samples need to be dispersed by an agitator. Then, the precipitations need to be filtered with a filter. Typically, an agitator costs \$1800 with an estimated annual treating capacity of 10 tonnes,[30] and a filter costs \$2000 with an estimated annual treating capacity of 10 tonnes.[31] Assuming their lifespan of 20 years, the capital cost in this process was calculated to be \$332.5 $tonne^{-1}$, \$780 $tonne^{-1}$, and \$70.3 $tonne^{-1}$ for pyrometallurgical, hydrometallurgical and direct recycling, respectively, when normalized by recycling 1 tonne of spent battery.

For the low-temperature calcination (~873 K) process, the capital expense is \$46.0 to treat one tonne of samples.[17] For the pyrometallurgical and hydrometallurgical routes, 0.88 tonne collected battery pieces from 1 tonne of spent battery were calcined. Thus, the capital cost was calculated to be \$40.9 $tonne^{-1}$ in this process. However, for direct recycling and RER, 0.37 tonne of cathode was separated from 1 tonne of spent cathode before calcination. The capital cost was calculated to be \$17.0 $tonne^{-1}$ in this process.

Similarly, for the high-temperature regeneration process, the capital expense is \$99.0 to treat one tonne of samples.[17] Corresponding, when normalized by recycling 1 tonne of spent battery (Fig. S52, ESI†), the capital cost was \$48.5 $tonne^{-1}$, \$46.5 $tonne^{-1}$, and \$39.6 $tonne^{-1}$ for pyrometallurgical, hydrometallurgical and direct recycling.

In the electrothermal heating process, the commercial arc welder costs \$130.[32] In our experiment, ~0.5 g cathode can be resynthesized in 30 s, corresponding to recycling ~1.2 g of spent battery (Fig. S52, ESI†). Thus, it was estimated that the annual recycling capacity was ~1 tonne. Assuming the life span of the equipment was 20 years, its capital expense can be calculated to be \$6.50 tonne^{-1}.

The detailed materials cost, energy cost in electricity, and capital cost are calculated and listed in Table S11 (ESI†). The total cost is calculated as the sum of the materials cost, energy cost, and capital cost. Other labor, sales, administration, and research expenses were estimated from the EverBatt2020 database[18] with a value of \$3.98 kg^{-1}.

The value of commercial LCO is \$57.25 kg$^{-1,}$ and the value of commercial high-voltage LCO is \$62.25 kg^{-1}.[33] The profit was calculated by subtracting the total cost and other expenses from the income, which were listed in Table S12 (ESI†).

5.6 Sensitivity and uncertainty.

There are some considerations and potential uncertainties in this study. Firstly, the energy consumption, GHG emission, water consumption, and price values of the feedstock used in this study were obtained from different sources. which may introduce some uncertainties. Secondly, several assumptions were made in this study regarding the material recycling and the processing parameters, such as calcination, agitation, and filtration, due to the lack of explicit processes in the literature These assumptions may contribute to uncertainty in the findings. Thirdly, although the scalability of the RER process has been proposed, there is some uncertainty in the predicted energy consumption when scaling up the RER process to a larger scale, including factors such as labor cost, capital cost, and operating cost. Consequently, it is essential to consider these uncertainties and limitations when interpreting the results, and further research and validation at larger scales will be necessary to provide more accurate assessments of energy consumption, cost, and overall feasibility of the RER process.

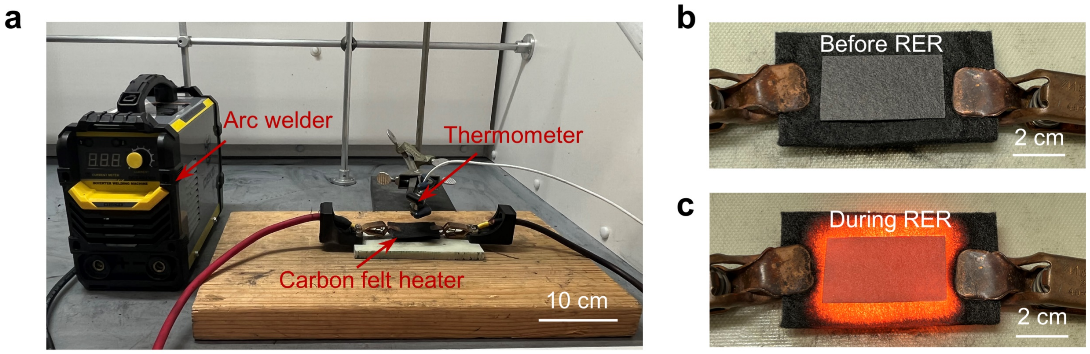

Fig. S1. Setup of RER system. (a) Picture of the RER reaction setup. (b) Zoom-in picture of the carbon felt heater before RER. (c) Zoom-in picture of the carbon felt heater during RER.

In this system, the commercial arc welder is applied as a power source and connected to a carbon felt. The carbon felt is functioned as an electric heater to load and heat reactant powders. The carbon felt was excavated to create a concave area for the powder sample loading, and carbon paper was put onto its surface to reduce the evaporation of reaction powers. An infrared thermometer is used for real-time temperature measurement. During the RER process, the concave area of the carbon felt with reduced cross-section area exhibits a higher resistance, leading to a localized heat for sample heating, based on Joule's law ($Q = I^2Rt$).

CAUTION:

To prevent the risk of electrical shock, it is required to follow safety guidelines when operating the equipment. We recommend adhering to the following safety guidelines when using this equipment. For additional safety practices, please refer to our previous publications.[34]

1. Enclose or insulate all wire connections securely.
2. Ensure all connections, wires, and components are suitable for high voltages and currents.
3. Be aware that component failure could cause high voltage to appear in unexpected places, such as heat sinks on the switching transistors.
4. Control wires should have opto-isolators rated for high voltage.
5. Avoid using toggle switches with metal toggles. If an arc develops, the metal toggle could become charged and pose a safety risk.
6. Follow the one-hand rule, with one hand working on the system and the other not touching any grounded surface.

7. Rotate the current knob to the minimum value of 0 after usage.
8. Turn off the circuit breaker switch behind the arc welder to disconnect the carbon felt holder from the power source after usage.
9. Arc welder should be unplugged and disconnected to the samples after usage.
10. Put up high voltage warning signs on the equipment.
11. Ensure to wear thick rubber gloves extending to the elbows to protect yourself from electrocution when using the equipment.
12. Safety glasses for welding are required to block the infrared and ultraviolet light during the electrothermal reaction.
13. The reliability and robustness of the RER system should be checked by an experienced electrical technician with weekly re-inspections.
14. All users should be properly trained by an experienced electrical technician.

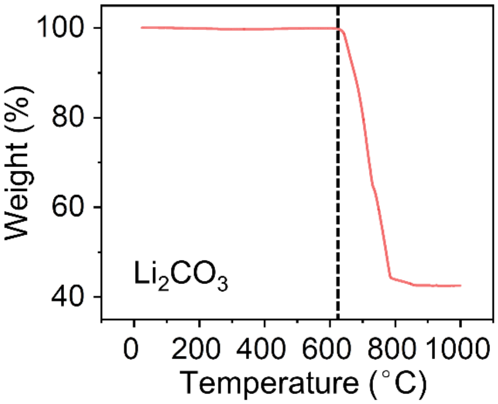

Fig. S2. TGA result of lithium carbonate. TGA was conducted in the air with a heating rate of 10 °C min^{-1}. It indicates that Li_2CO_3 begins to decompose at the temperature of ~620 °C.

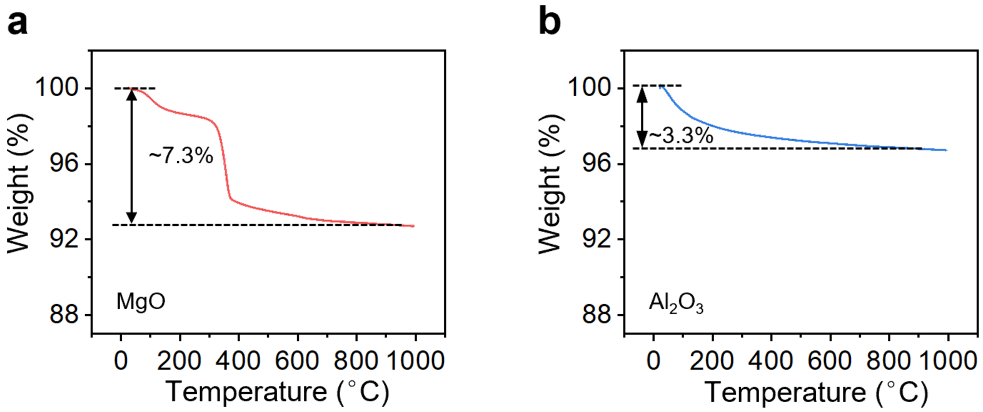

Fig. S3. TGA results of different dopants. (a) MgO, (b) Al_2O_3. TGA was conducted in 100 mL min^{-1} air with a heating rate of 10 °C min^{-1}.

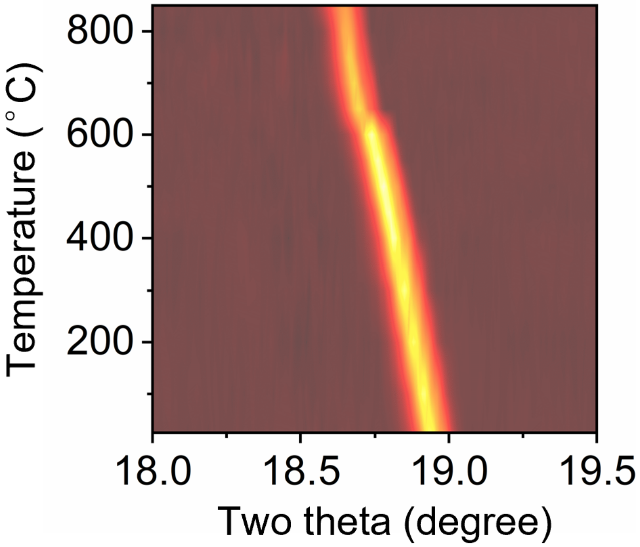

Fig. S4. Contour plot of temperature-dependent XRD pattern of s-LCO mixed with MgO (2 wt%) and Al_2O_3 (1 wt%). A distinct downshift of the (003) peak in the temperature range of 600-700 °C indicates the Mg/Al insertion temperature is ~650 °C.

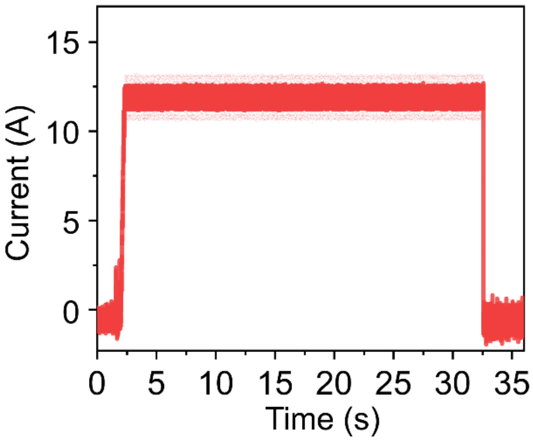

Fig. S5. Current profiles during the RER process. The real current is ~12 A, consistent with the set value. It indicates the stability of the current input of the arc welder system.

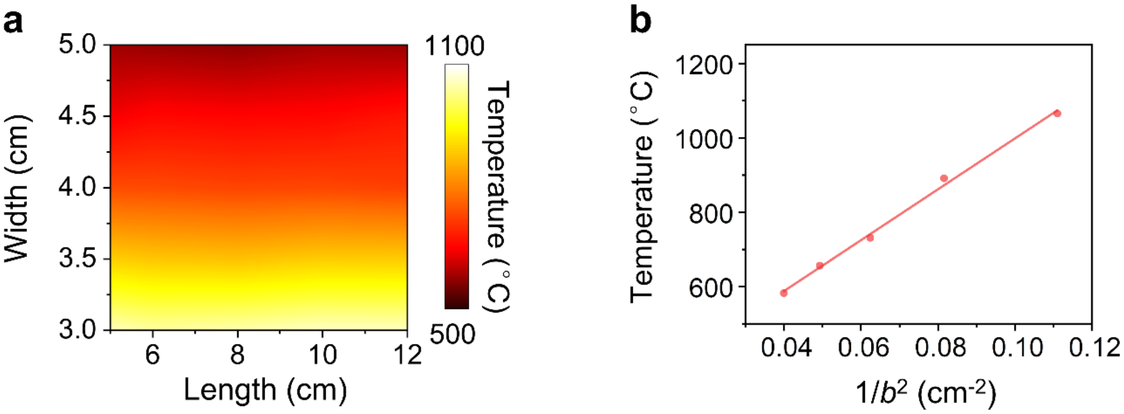

Fig. S6. Relationship between carbon felt size and stable electric heating temperature. (a) Heating temperature mapping of the carbon felt with different widths and lengths. (b) Relationship between heating temperature with the felt width. The input current was set as 12 A. The heating temperature has a negligible relationship with felt length, but it is proportional to $1/b^2$, which is consistent with the theoretical calculation in Note S1.

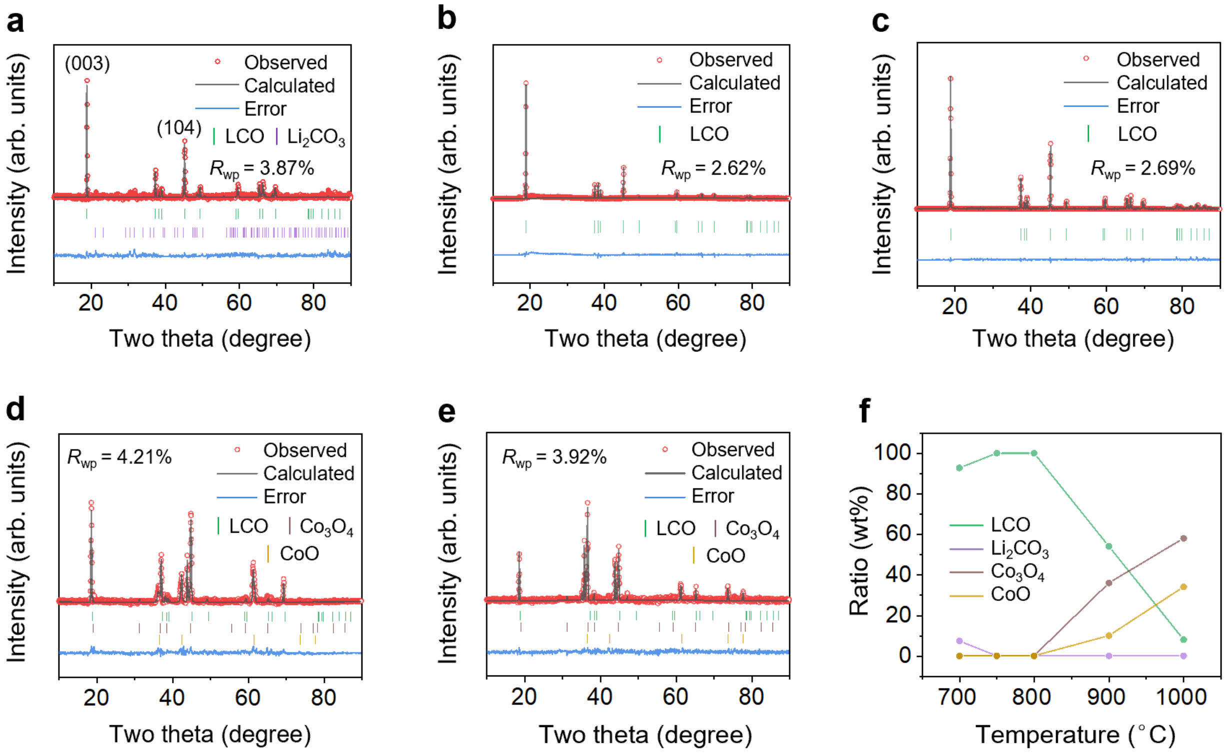

Fig. S7. XRD patterns of r-LCO treated under different temperatures. (a-e) XRD Rietveld refinement results of r-LCO treated under (a) 700 °C. (b) 750 °C. (c) 800 °C. (d) 900 °C. (e) 1000 °C. (f) Composition ratios of r-LCO treated under different temperatures.

For r-LCO treated under 700 °C, distinct Li_2CO_3 peaks in XRD patterns demonstrate incomplete lithiation. On the contrary, with a higher temperature higher than 900 °C, LCO tends to degrade into Co_3O_4 and CoO. Therefore, 750 °C was chosen as the optimized temperature for LCO regeneration.

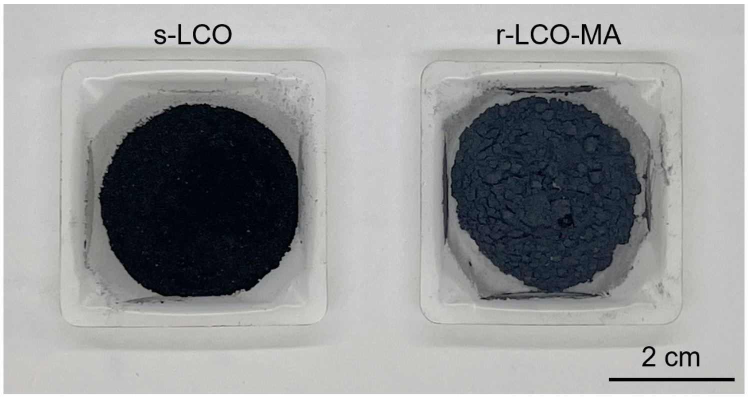

Fig. S8. Pictures of s-LCO (left) and r-LCO (right). These LCO samples were collected from 2-batch treatment, and 500 mg of samples were treated per batch.

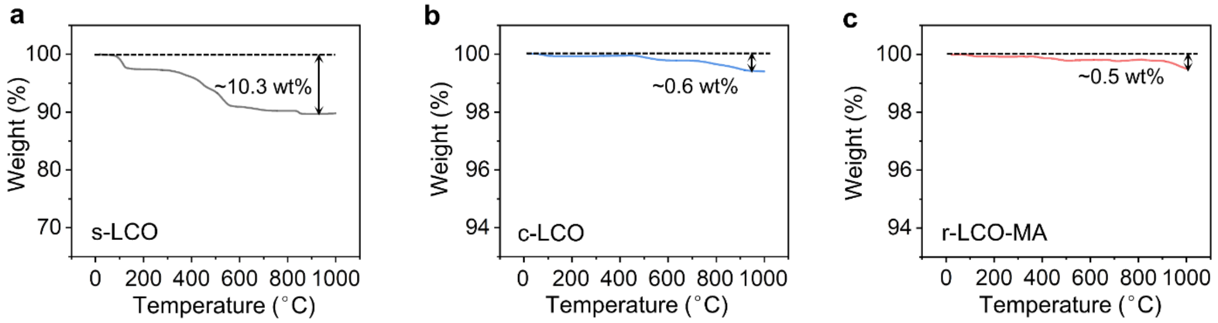

Fig. S9. TGA results of different LCO samples. (a) s-LCO. (b) c-LCO. (c) r-LCO-MA. TGA was conducted in the air with a heating rate of 10 °C min^{-1}.

The weight loss of ~10 wt% of spent LCO comes from the decomposition of CEI and binder, and the oxidation of conductive carbon. While in r-LCO-MA, the weight loss was low to ~0.5 wt% under 1000 °C, comparable to that of c-LCO (~0.6 wt%). It indicates the complete removal of the impurities and complete decomposition of lithium carbonate precursors during RER process.

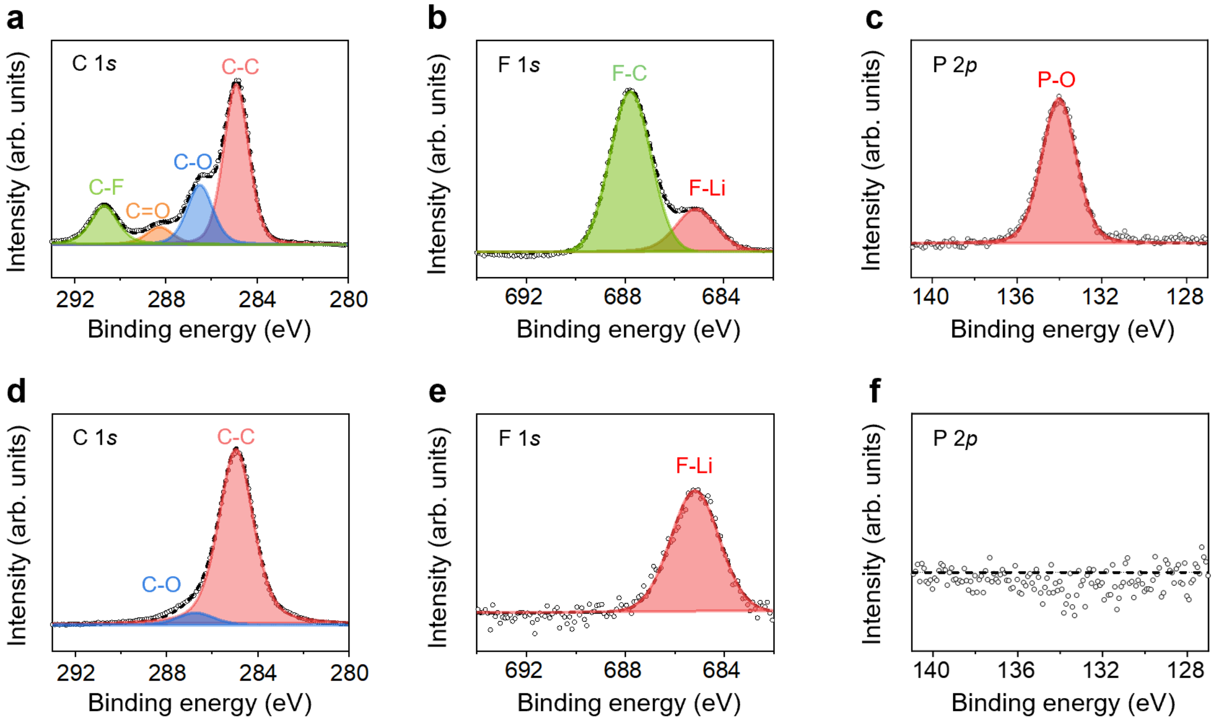

Fig. S10. XPS spectra of s-LCO before and after preheat treatment. (a) C 1*s* spectra of s-LCO. (b) F 1*s* spectra of s-LCO. (c) P 2*p* spectra of s-LCO. (d) C 1*s* spectra of annealed s-LCO. (e) F 1*s* spectra of annealed s-LCO. (f) P 2*p* spectra of annealed s-LCO.

For the s-LCO, the C 1*s* spectrum exhibited distinct peaks corresponding to C=O and C–O bonds, attributed to residual carbonate electrolytes, along with a C–F peak from the binder. The F 1*s* spectrum revealed an F–Li peak from decomposed $LiPF_6$, and an F–C peak originating from the binder. In P 2*p* spectra, a P-O peak was identified, which we attributed to $LiPO_xF_y$ species formed from decomposed electrolytes.

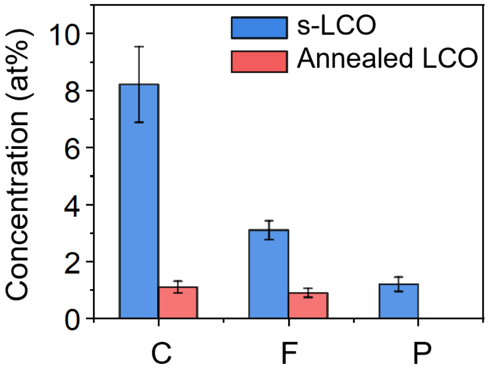

Fig. S11. Impurity element contents before and after preheat treatment (600 °C in the air for 2 h) tested by XPS. The error bars denote the standard deviation where $N = 3$.

After annealing, the organic binder and electrolyte residues were effectively removed, as evidenced by a distinct reduction in carbon content from 8.2 at% to 1.1 at%. The remaining carbon was primarily due to hydrocarbon adsorption from the air. Similarly, the fluorine content decreased from 3.1 at% to 0.9 at%, and phosphorus was reduced from 1.2 at% to below the detection limit.

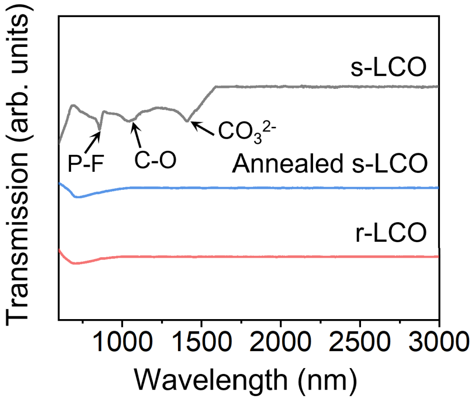

Fig. S12. FT-IR spectra of s-LCO (gray), annealed s-LCO (blue), and r-LCO (red).

The s-LCO displayed characteristic peaks at ~860 cm^{-1} (P–F), ~1050 cm^{-1} (C–O), and ~1410 cm^{-1} (carbonate). After annealing, these signals disappeared, consistent with the XPS results (Fig. S10, ESI†) and demonstrating the effective elimination of impurities from the cathode-electrolyte interphase (CEI) and electrolyte remnants.

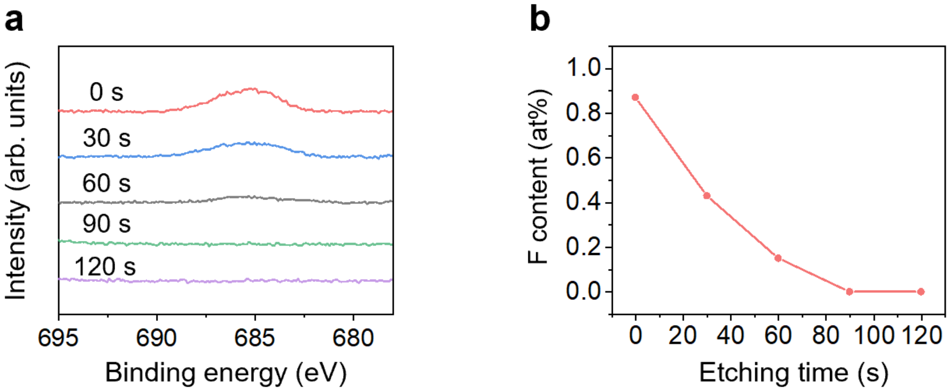

Fig. S13. XPS depth analysis of F for r-LCO-MA. (a) XPS F 1*s* spectra with different etching times. (b) F atomic ratios with different etching times. Considering that the etching rate was calibrated using Ta_2O_5 at 6 nm s^{-1}, the F doping depth is calculated to be ~9 nm.

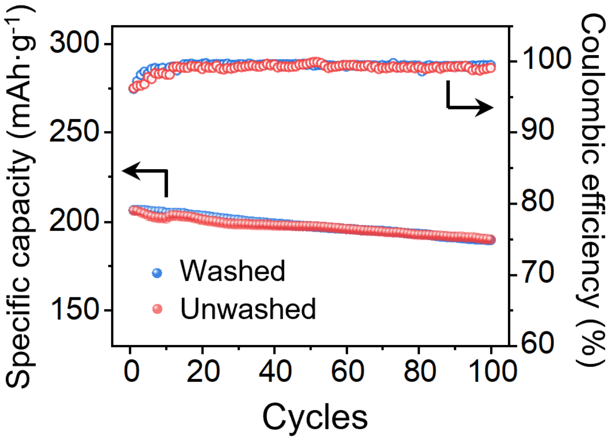

Fig. S14. Cycling stability of r-LCO-MA with (blue) and without prewashing step (red) at 0.2 C. The prewashing step involved soaking 1 g of s-LCO powder in 10 mL NMP for 24 h before undergoing the same annealing and RER process. After RER, r-LCO with and without N-methylpyrrolidone (NMP) washing exhibited a similar capacity retention of 92% after 100 cycles at 0.2 C in the cycling voltages of 3.0-4.6 V (Fig. S14), indicating that the washing step of s-LCO is not necessary for the RER process.

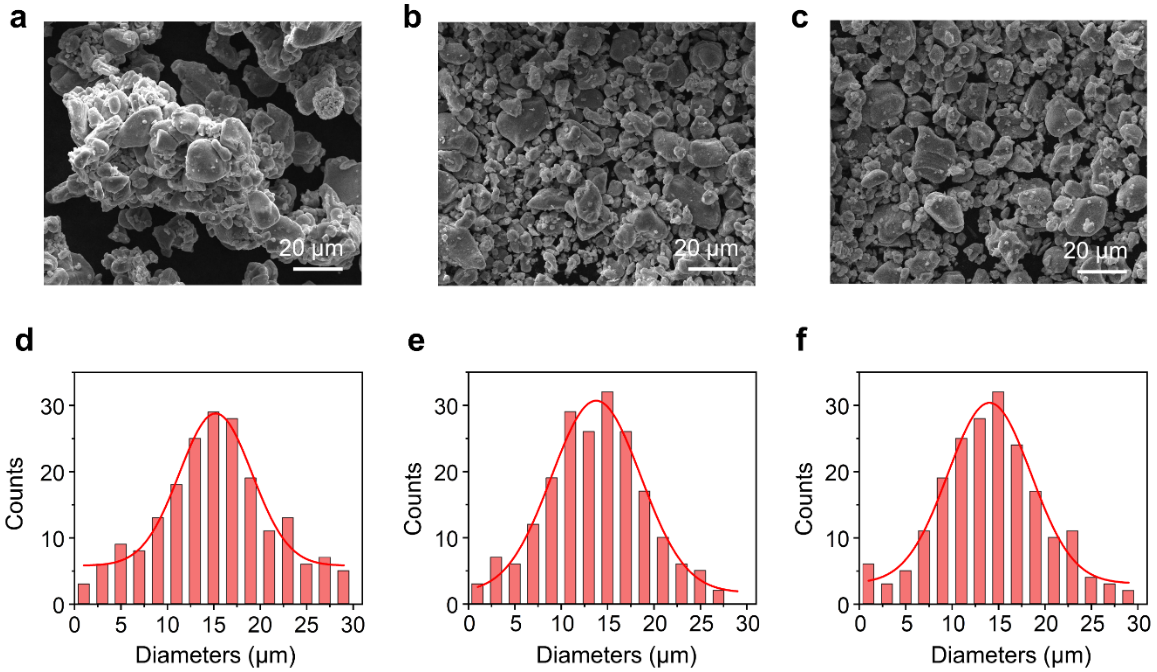

Fig. S15. Particle size of different LCO samples. a-c) SEM images of (a) s-LCO, (b) c-LCO, and (c) r-LCO-MA. d-f) Statistical particle distributions of (d) s-LCO, (e) c-LCO, and (f) r-LCO-MA. 200 particle diameters were counted for each LCO sample, respectively.

No obvious changes in LCO particle sizes were observed after RER. However, the particle agglomeration was released after the treatment, benefitting the complete lithiation.

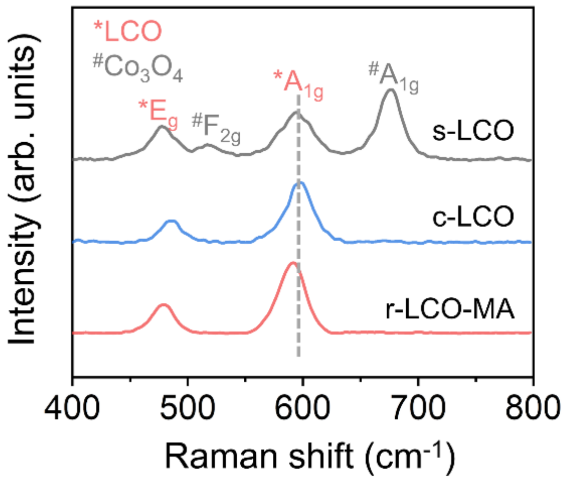

Fig. S16. Raman spectra of s-LCO, c-LCO, and r-LCO-MA.

The disappearance of Co_3O_4 peaks in Raman spectra indicates the restored layer structure during the RER process. The E_g and A_{1g} modes of r-LCO-MA both shift to lower wavenumbers, indicating an increase in its c-axis lattice parameter compared to c-LCO.

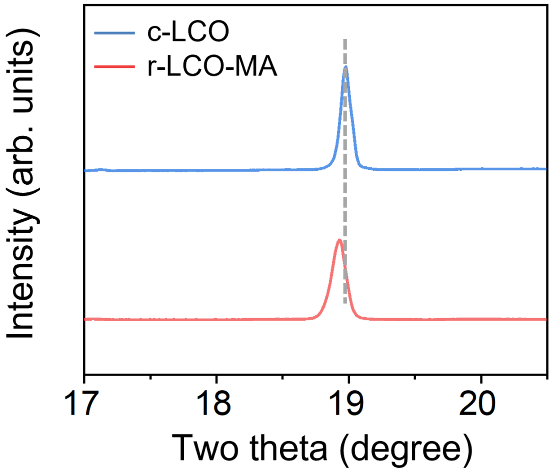

Fig. S17. High-resolution XRD patterns of c-LCO, and r-LCO-MA. The downshift of the (003) peak of r-LCO-MA compared with that of c-LCO indicates the slightly increased interlayer distance due to the Mg/Al insertions.

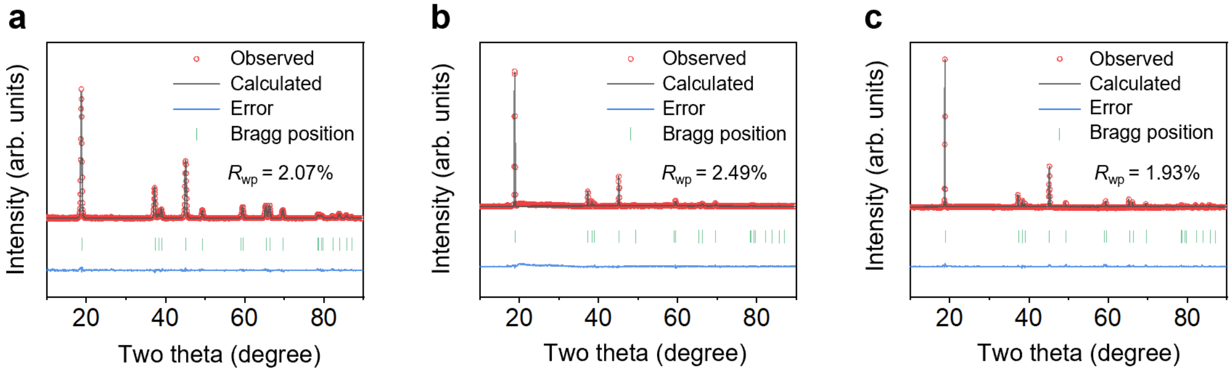

Fig. S18. XRD Rietveld refinement results for (a) s-LCO, (b) c-LCO, and (c) r-LCO-MA.

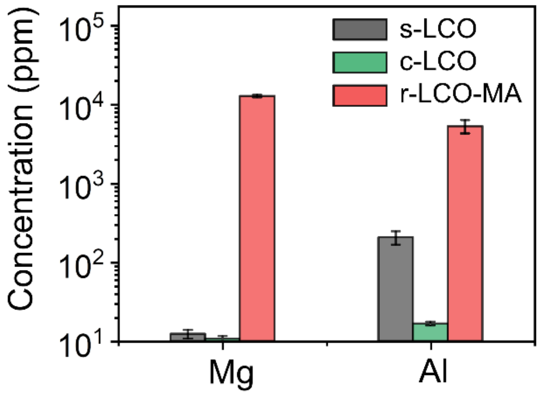

Fig. S19. Mg and Al contents in s-LCO, c-LCO, and r-LCO-MA. The contents of Mg and Al in s-LCO are several orders of magnitude lower than r-LCO-MA, indicating that the doped Mg and Al in r-LCO come from additional added precursors.

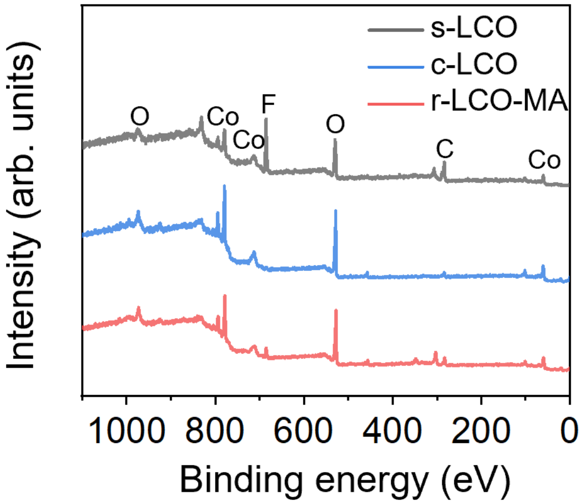

Fig. S20. XPS full spectra of s-LCO (grey), c-LCO (blue), and r-LCO-MA (red).

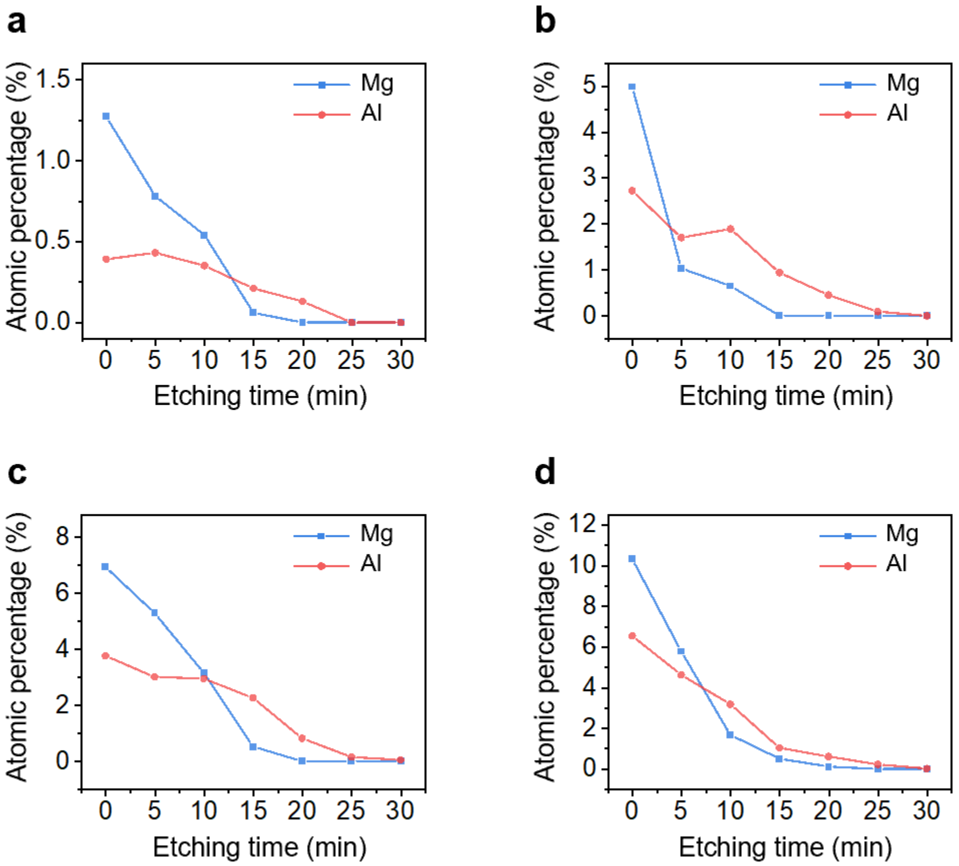

Fig. S21. XPS depth analysis of Mg (blue) and Al (red) for r-LCO-MA with different doping content. (a) 0.4 wt% MgO and 0.2 wt% Al_2O_3. (b) 2 wt% MgO and 1 wt% Al_2O_3. (c) 4 wt% MgO and 2 wt% Al_2O_3. (d) 6 wt% MgO and 3 wt% Al_2O_3.

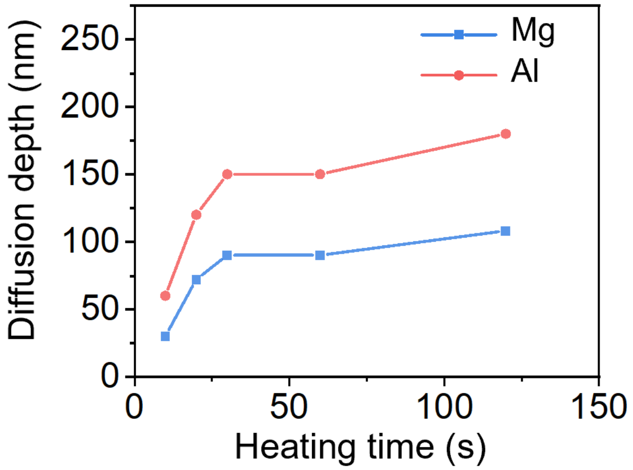

Fig. S22. Diffusion depth of Mg (blue) and Al (red) on r-LCO-MA surface with different etching times. The etching rate was calibrated using Ta_2O_5 at 6 nm s^{-1}. The diffusion depth was determined by multiplying the etching rate by the etching time when the element content fell below the detection limit.

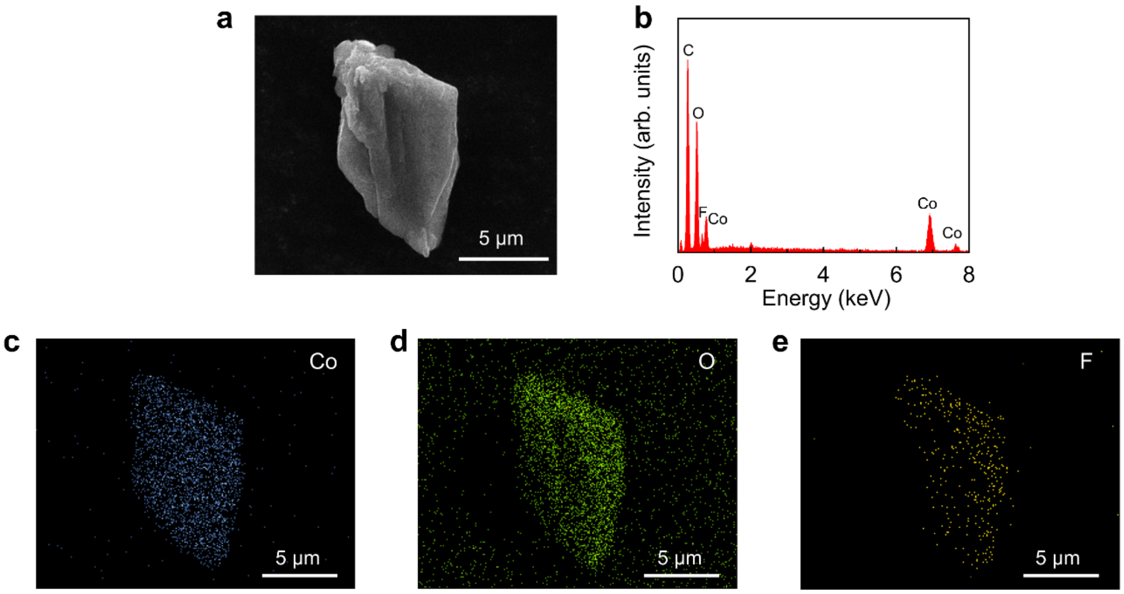

Fig. S23. SEM and EDS mapping of s-LCO particles. (a) SEM image of LCO particle. (b) EDS spectrum of s-LCO. c-e) EDS mapping of (c) Co, (d) O, and (e) F.

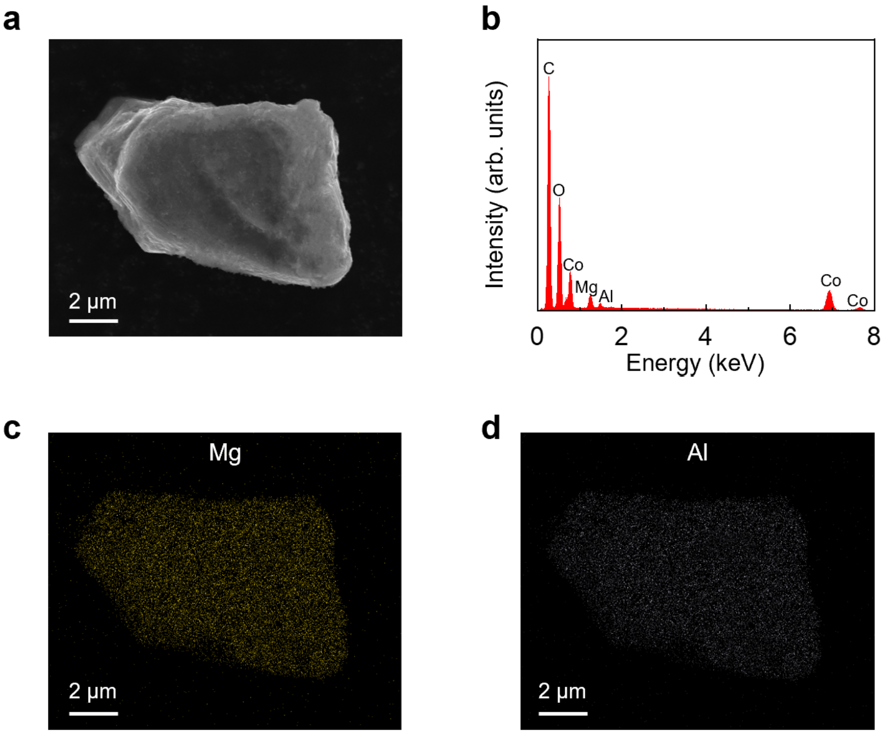

Fig. S24. SEM image and corresponding element distributions of r-LCO-MA with 9 wt% doping. (a) SEM image. (b) Mg distribution. (c) Al distribution.

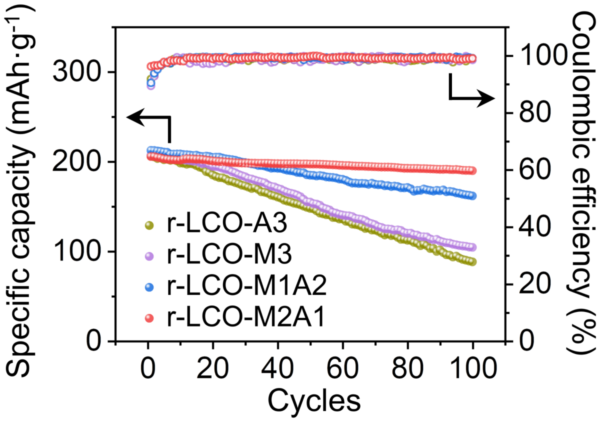

Fig. S25. Cycling stability for 100 cycles of r-LCO-A3 (dark yellow), r-LCO-M3 (purple), r-LCO-M1A2 (blue) and r-LCO-M2A1 (red). Here, A denotes Al, and M denotes Mg. The number after M/A indicates the input MgO/Al_2O_3 mass ratios in the precursors before RER.

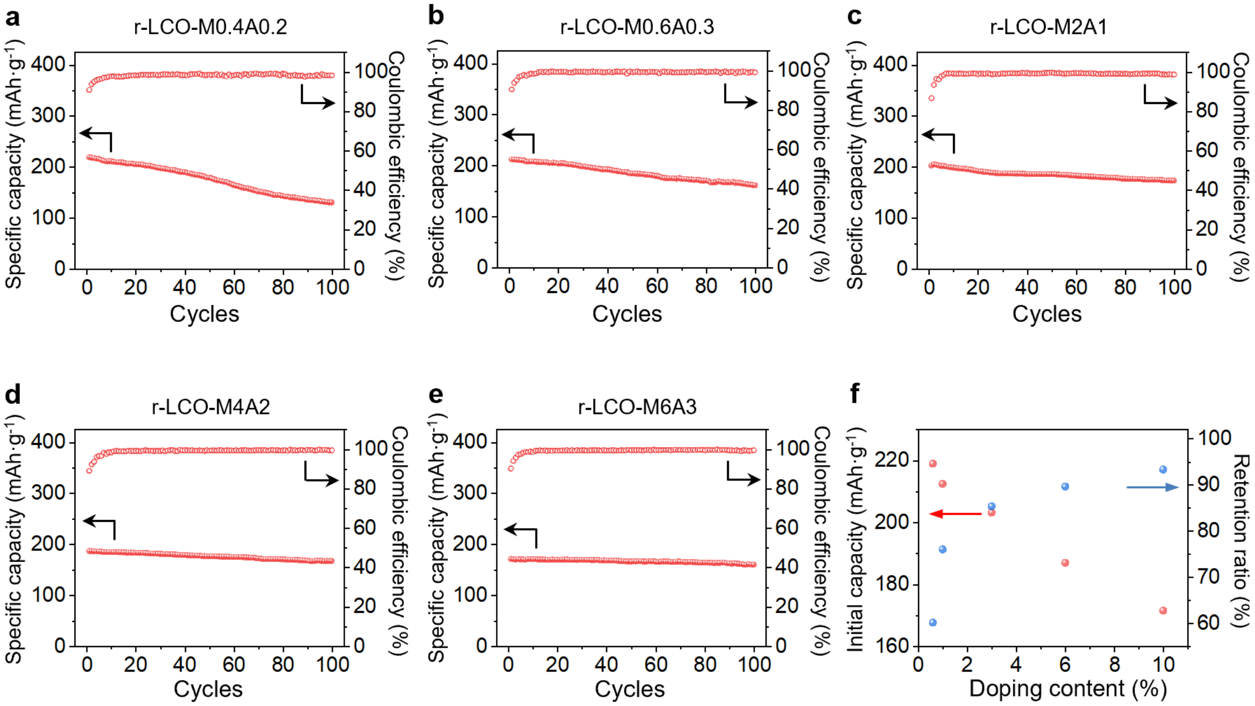

Fig. S26. Cycling stability of r-LCO with different Mg/Al doping contents. (a) r-LCO-M0.4A0.2. (b) r-LCO-M0.6A0.3. (c) r-LCO-M2A1. (d) r-LCO-M4A2. (e) r-LCO-M6A3. (f) Relationship between the initial capacity, capacity retention ratio, and the doping content. The initial input MgO/Al_2O_3 mass ratio is kept at 2:1.

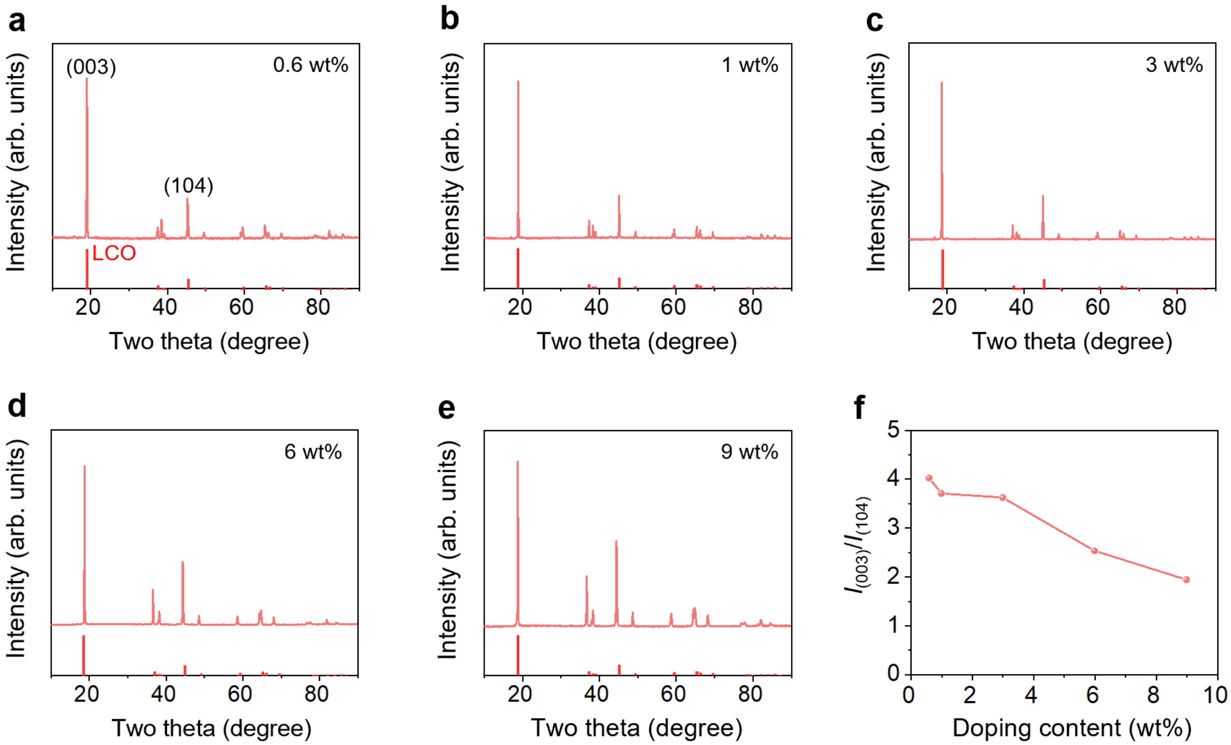

Fig. S27. XRD patterns of r-LCO with different Mg/Al doping contents. (a) 0.6 wt%. (b) 1 wt%. (c) 3 wt%. (d) 6 wt%. (e) 9 wt%. (f) Intensity ratio between (003) and (104) peaks of r-LCO with different doping contents. The PDF reference card for LCO is 04-013-9887.

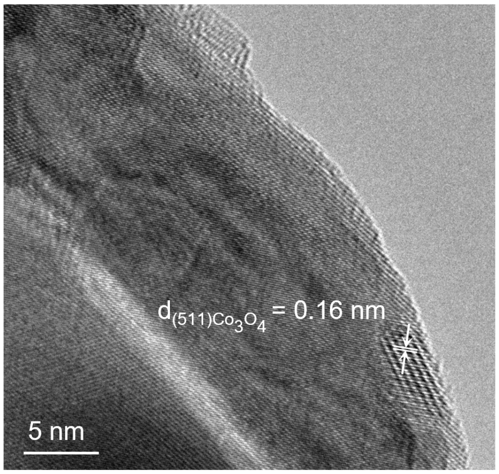

Fig. S28. TEM image of r-LCO-MA with 9 wt% Mg/Al doping.

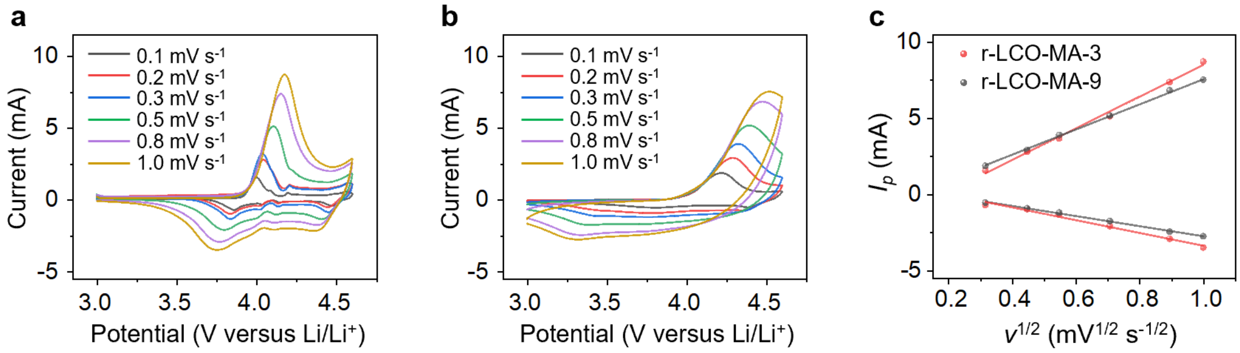

Fig. S29. CV curves of r-LCO-MA. (a) CV curves with different scan rates of r-LCO-MA with 3 wt% doping content. (b) CV curves with different scan rates of r-LCO-MA with 9 wt% doping content. (c) Li^+ diffusion coefficient of r-LCO-MA with 3 wt% (red line) and 9 wt% (gray line).

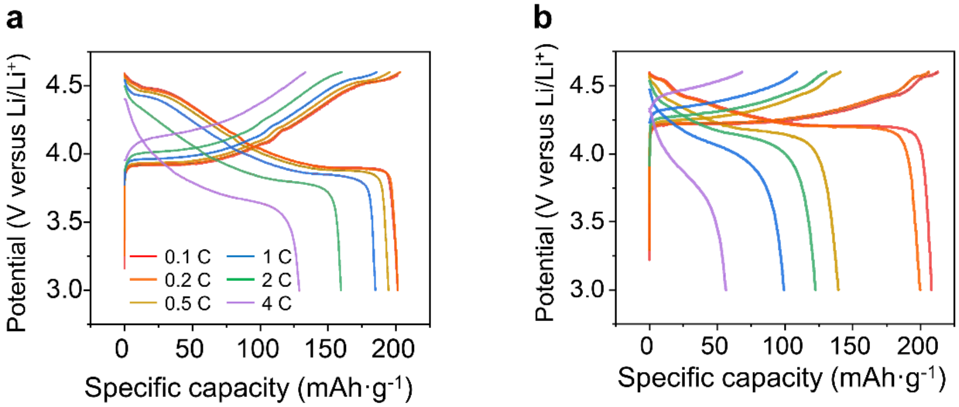

Fig. S30. Charge and discharge curves at different rates. (a) r-LCO-MA. (b) c-LCO.

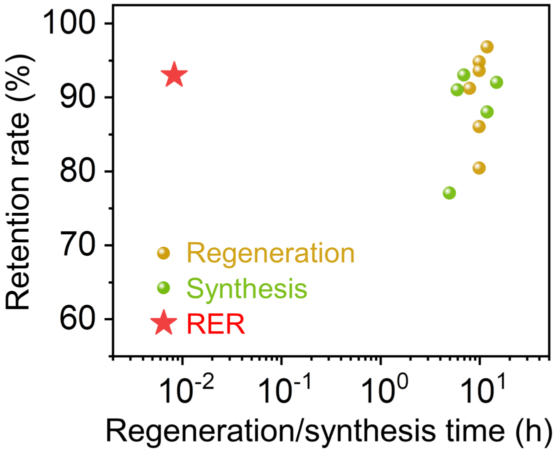

Fig. S31. Comparisons of LCO synthesis/regeneration time and LCO cathode capacity retention ratio after 100 cycles between RER process with other regeneration[16,35-39] and synthesis[40-44] methods.

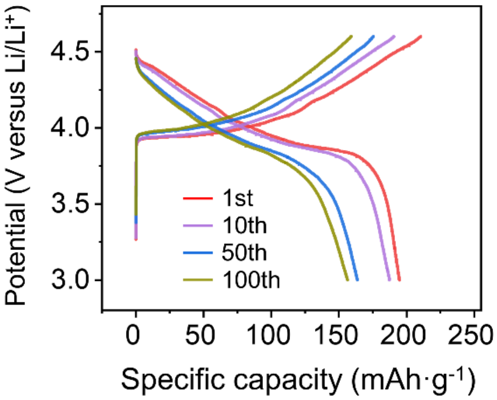

Fig. S32. Charge and discharge curves for the full-cell battery at 0.2 C. r-LCO-MA is used as the cathode and commercial graphite as the anode. The battery cycles at 0.1 C for 10 cycles before further cycling at 0.2 C.

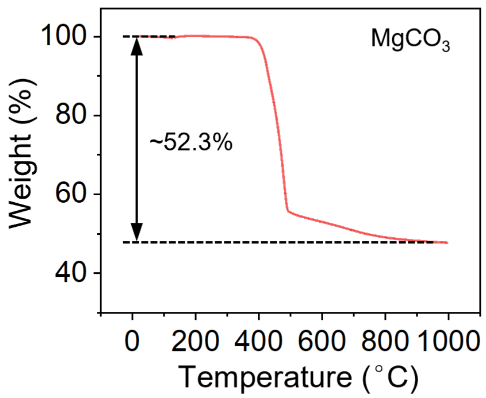

Fig. S33. TGA results of $MgCO_3$. TGA was conducted in 100 mL min^{-1} air with a heating rate of 10 °C min^{-1}.

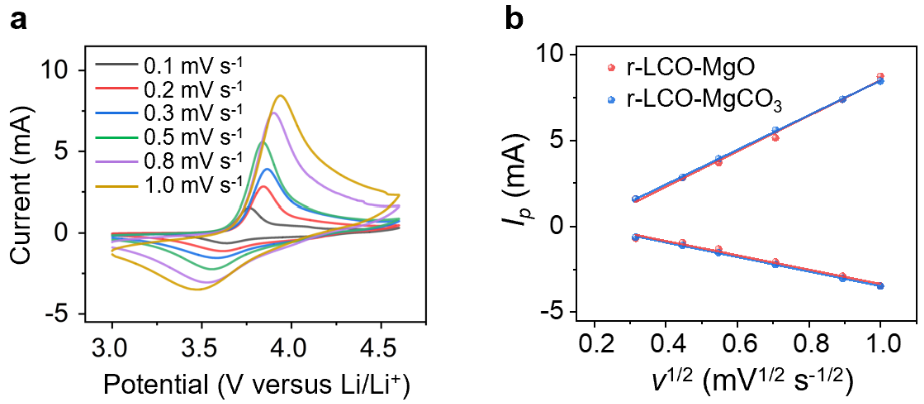

Fig. S34. CV results for r-LCO using 4.2 wt% $MgCO_3$ and 1.0 wt% Al_2O_3 as the dopants. (a) CV curves at different scan rates in a potential window of 3.0–4.6 V versus Li/Li$^+$. (b) Comparison of Li$^+$ diffusion coefficients of r-LCO-MA with MgO (red line) and $MgCO_3$ as the Mg dopant (blue line).

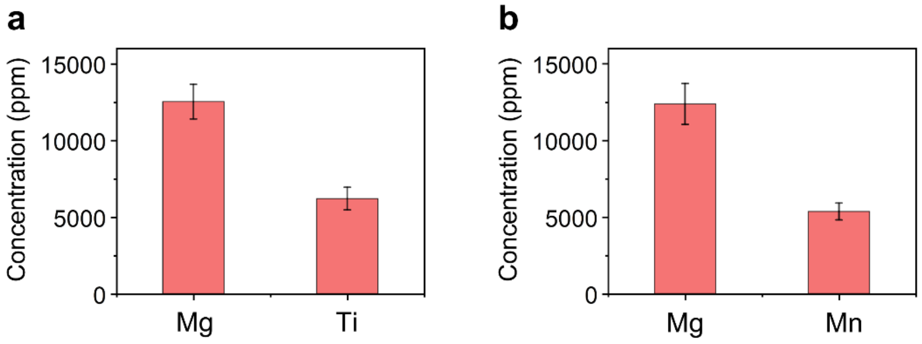

Fig. S35. Doping element contents in different r-LCO samples. (a) Mg/Mn co-doping (r-LCO-M2M1). (b) Mg/Ti co-doping (r-LCO-M2T1).

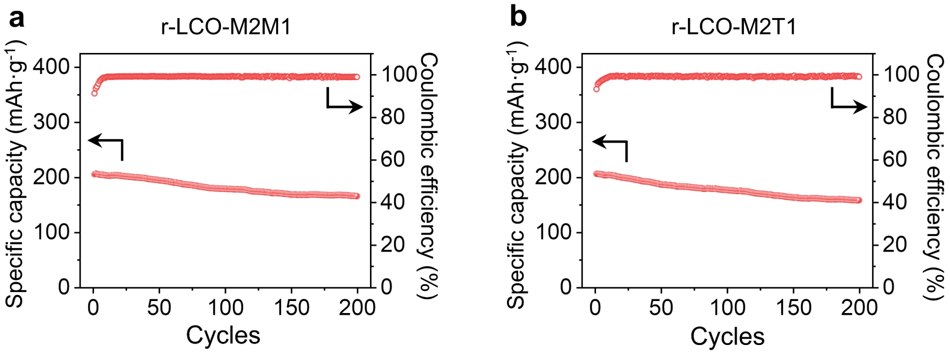

Fig. S36. Cycling stability of r-LCO with other metal doping. (a) Mg/Mn co-doping. (b) Mg/Ti co-doping.

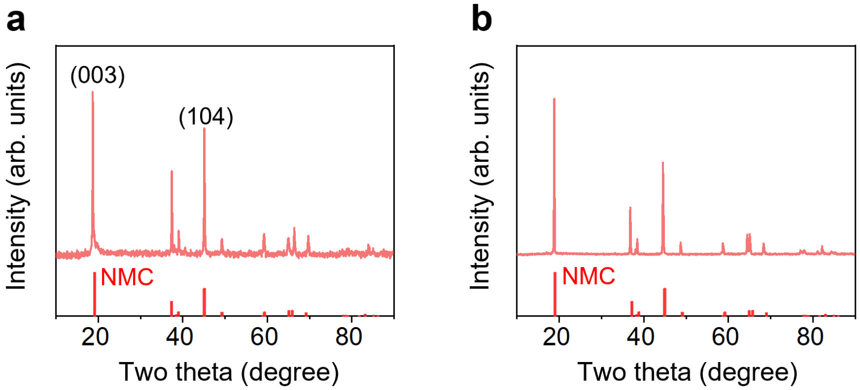

Fig. S37. XRD patterns of the s-NMC and r-NMC-MA. (a) XRD pattern of s-NMC. (b) XRD pattern of r-NMC-MA. The PDF reference card for NMC111 is 01-086-8822.

The rejuvenated NMC111 with 2 wt% MgO and 1 wt% Al_2O_3 doping, denoted as r-NMC-MA, exhibited structural improvements, as evidenced by the increased intensity ratio between the (003) and (104) peaks (*I*(003)/*I*(104)) from 1.28 to 1.69 in XRD patterns. This indicated improved crystallinity and structure restoration (Fig. S37).

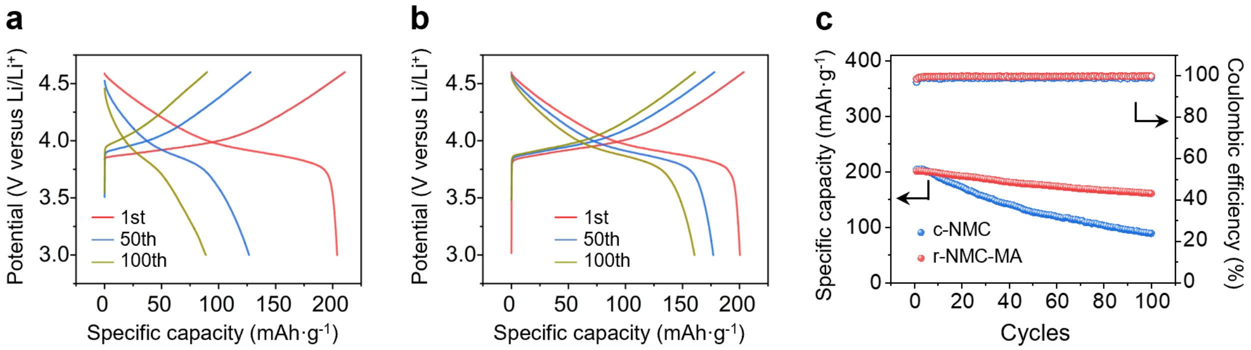

Fig. S38. Cycling performance of c-NMC and r-NMC-MA. (a) Charge-discharge profiles at different cycles for c-NMC. (b) Charge-discharge profiles at r-NMC-MA. (c) Cycling stability of c-NMC (blue spot) and r-NMC-MA anode (red spot) at 0.2 C.

In a voltage range of 3.0–4.6 V, r-NMC-MA demonstrated improved cycling stability, retaining 90% of its initial capacity (201 mAh g^{-1}) after 200 cycles at 0.2 C. On the contrary, commercial NMC111 (denoted as c-NMC) exhibited only 44% capacity retention (Fig. S38). These results highlight the role of Mg/Al doping in enhancing high-voltage stability.

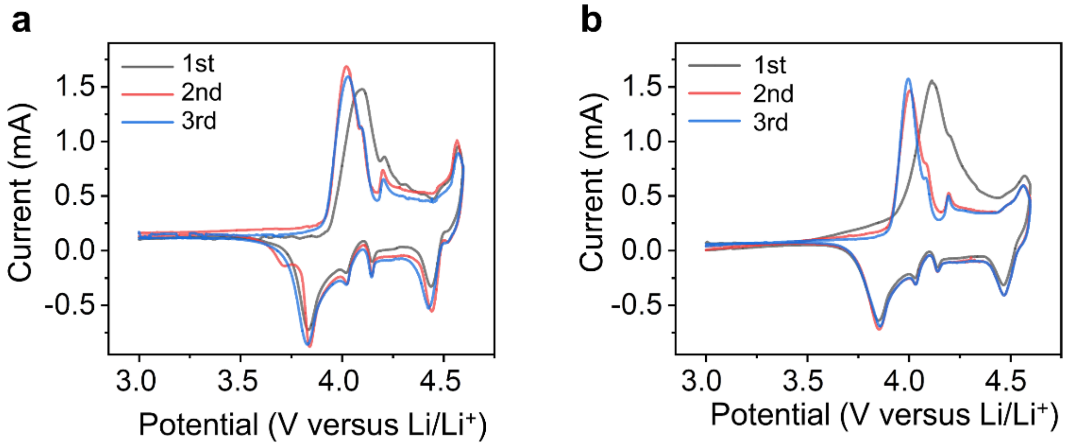

Fig. S39. Cyclic voltammetry (CV) curves in a potential window of 3.0–4.6 V versus Li/Li$^+$ collected at a scan rate of 100 μV s^{-1} for 3 cycles. (a) c-LCO. (b) r-LCO-MA.

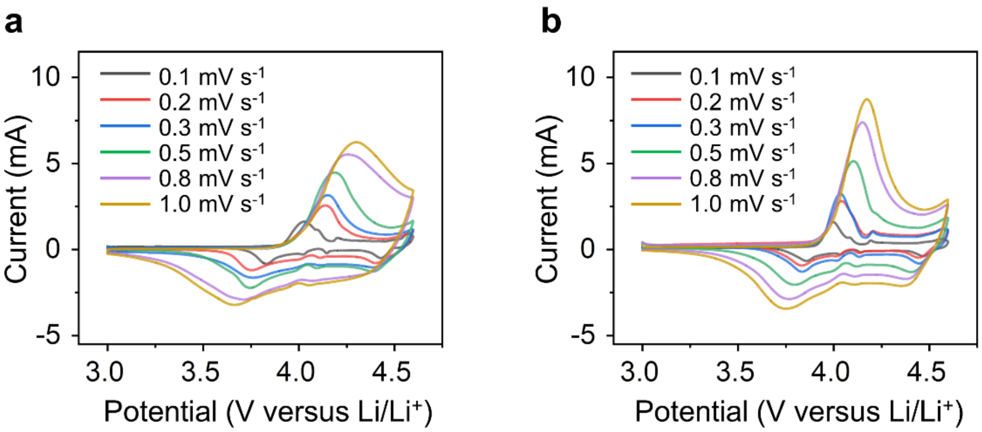

Fig. S40. CV curves at different scan rates in a potential window of 3.0–4.6 V versus Li/Li$^+$. (a) c-LCO. (b) r-LCO-MA.

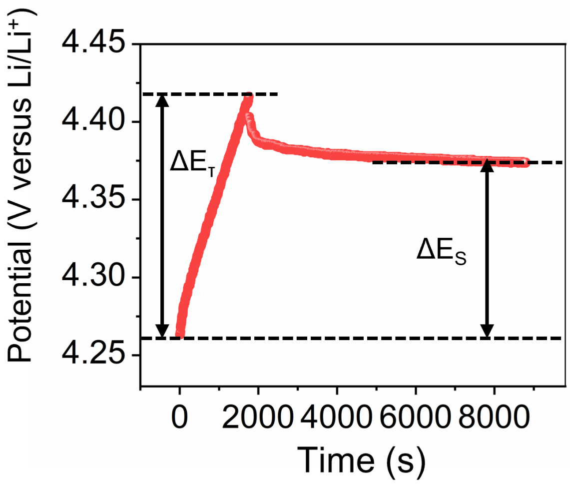

Fig. S41. Schematic illustration of a signal step of the GITT measurement during the charging process.

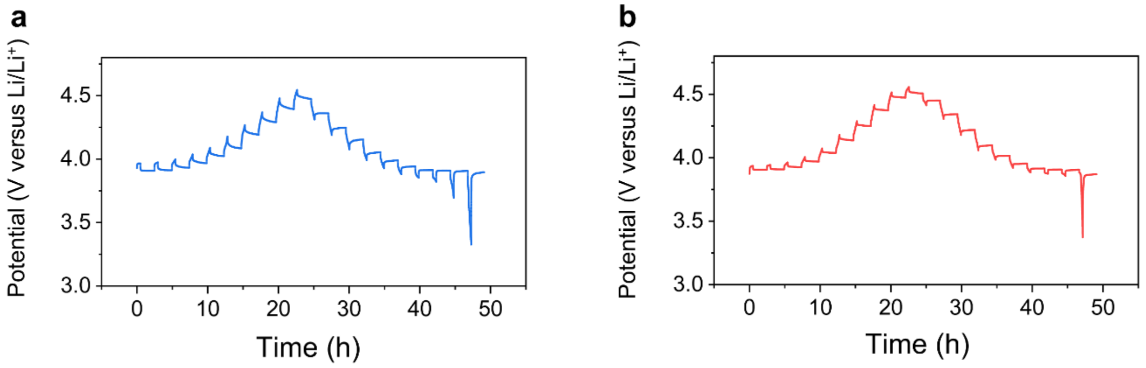

Fig. S42. GITT profiles of the LCO cathode materials at 0.2 C. (a) r-LCO-MA. (b) c-LCO.

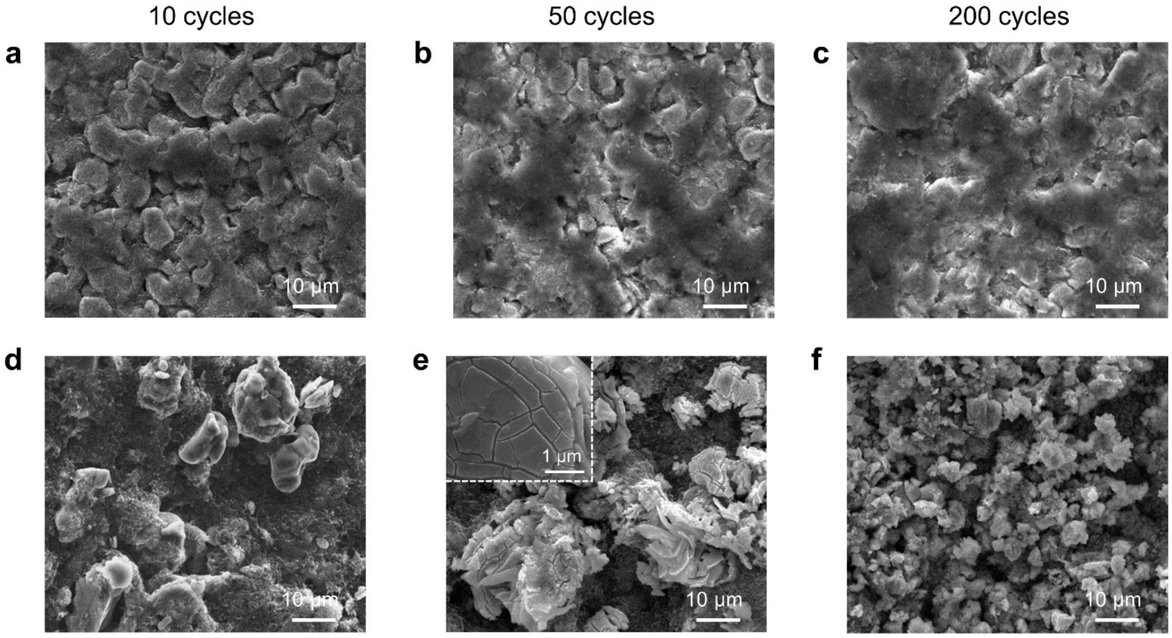

Fig. S43. Morphology of LCO cathode after cycling from 3.0 to 4.6 V for different cycles. (a-c) r-LCO-MA for (a) 10 cycles, (b) 50 cycles, and (c) 200 cycles. (d-f) c-LCO for (d) 10 cycles, (e) 50 cycles (Inset: zoom-in image of the crack LCO particle), and (f) 200 cycles.

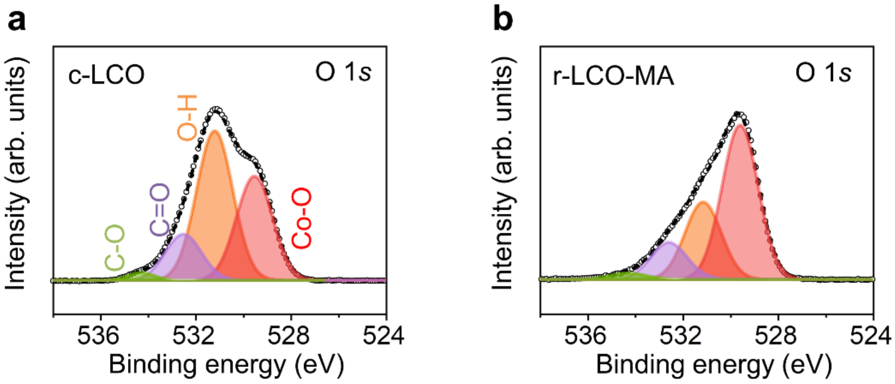

Fig. S44. O 1*s* XPS spectra of LCO cathodes after 200 cycles. (a) c-LCO. (b) r-LCO-MA.

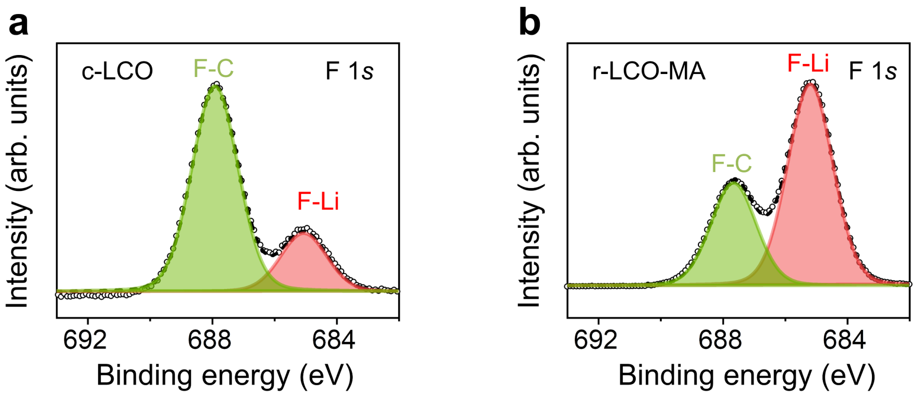

Fig. S45. F 1*s* XPS spectra of LCO cathodes after 200 cycles. (a) c-LCO. (b) r-LCO-MA.

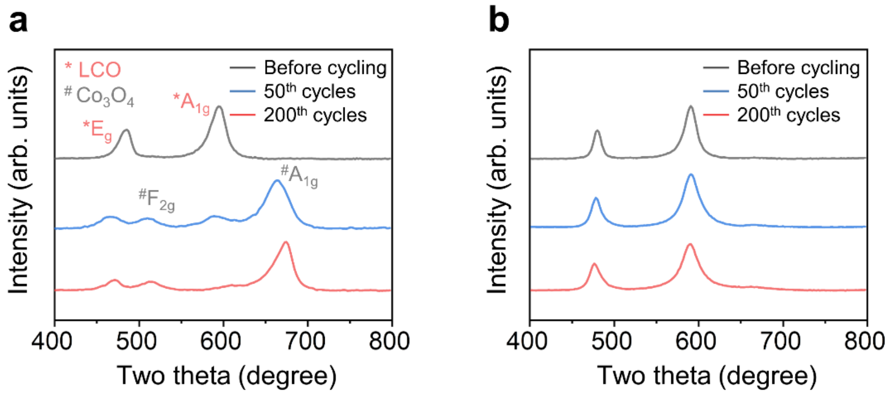

Fig. S46. Raman spectra after cycling from 3.0 to 4.6 V for different cycles. (a) c-LCO. (b) r-LCO-MA.

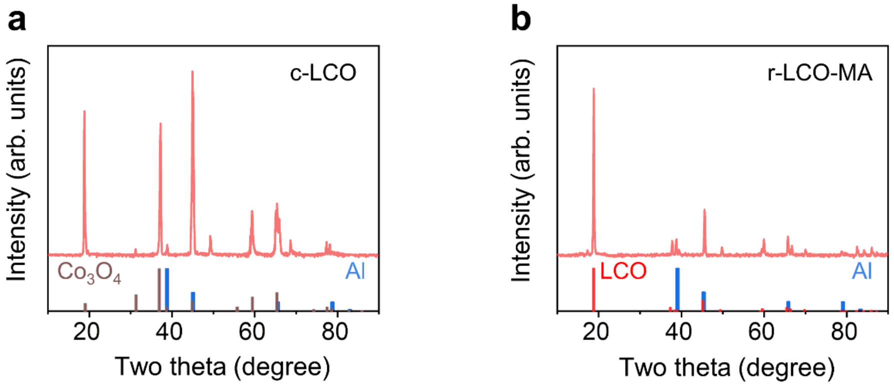

Fig. S47. XRD patterns of LCO cathodes after cycling for 200 cycles. (a) c-LCO. (b) r-LCO-MA. The PDF reference cards for each are 04-013-9887 (LCO), 04-013-9887 (Li_2CO_3), 00-009-0418 (Co_3O_4), and 01-071-4625 (Al).

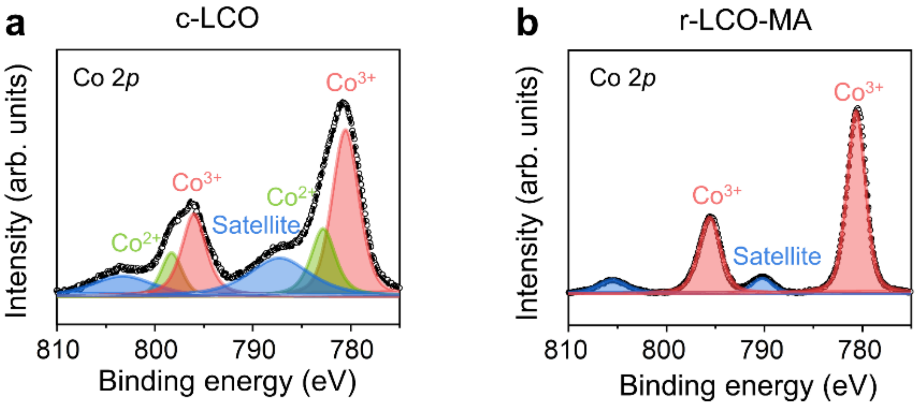

Fig. S48. Co 2*p* XPS spectra of LCO cathodes after cycling for 200 cycles. (a) c-LCO. (b) r-LCO-MA.

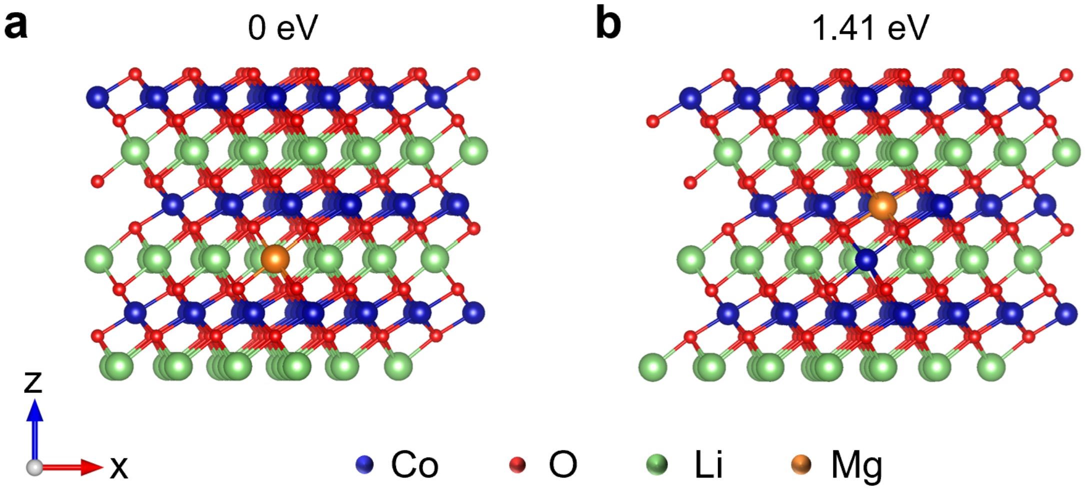

Fig. S49. Simulated energy barriers for Mg doping at different sites in LCO. (a) Site 1: a Mg atom directly occupies a Li vacancy. (b) Site 2: a Co atom is displaced into a Li vacancy by a substituting Mg atom. The LCO supercell consisted of $Li_{46}Co_{48}O_{96}$ with two Li vacancies. The doping energies are normalized to the configuration where Mg directly occupies a Li vacancy. The energy for Mg at site 1 is 1.41 eV lower than that at site 2, indicating that Mg tends to directly occupy a Li vacancy.

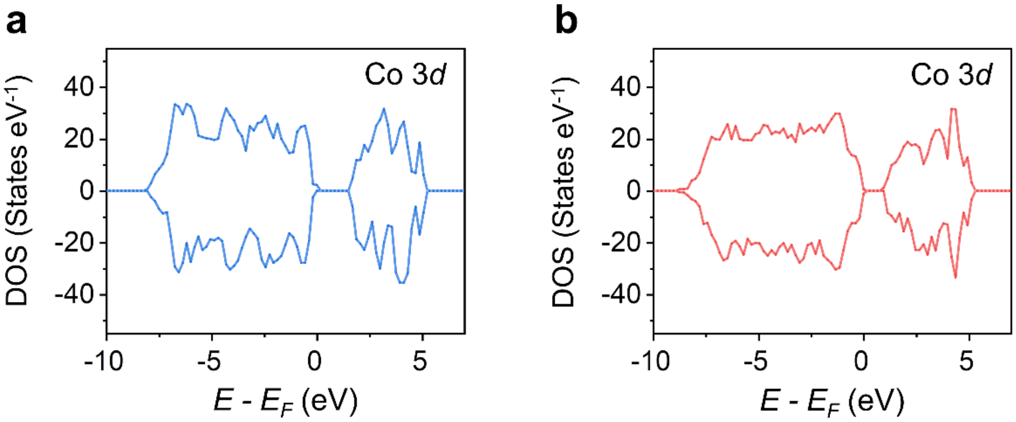

Fig. S50. Co 3*d* projected density of states (pDOS) of $Li_{0.2}CoO_2$. (a) Li9Co48O9. (b) Li9Mg2AlCo48O9.

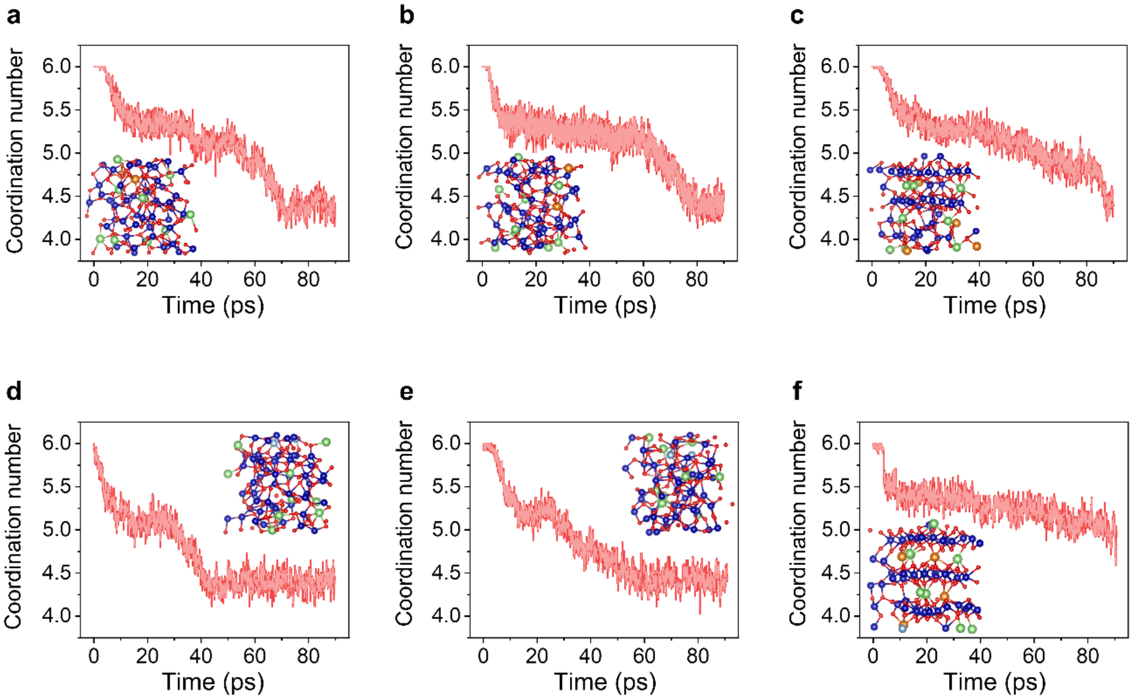

Fig. S51. Simulated variation of Co coordination in $Li_{0.2}CoO_2$ matrix with different content doping. (a) Li9Mg2Co48O9. (b) Li9Mg3Co48O9. (c) Li9Mg4Co48O9. (d) Li9Al2Co48O9. (e) Li9Al3Co48O9. (f) Li9Mg4Al2Co48O9. Insets are corresponding optimized structure snapshots.

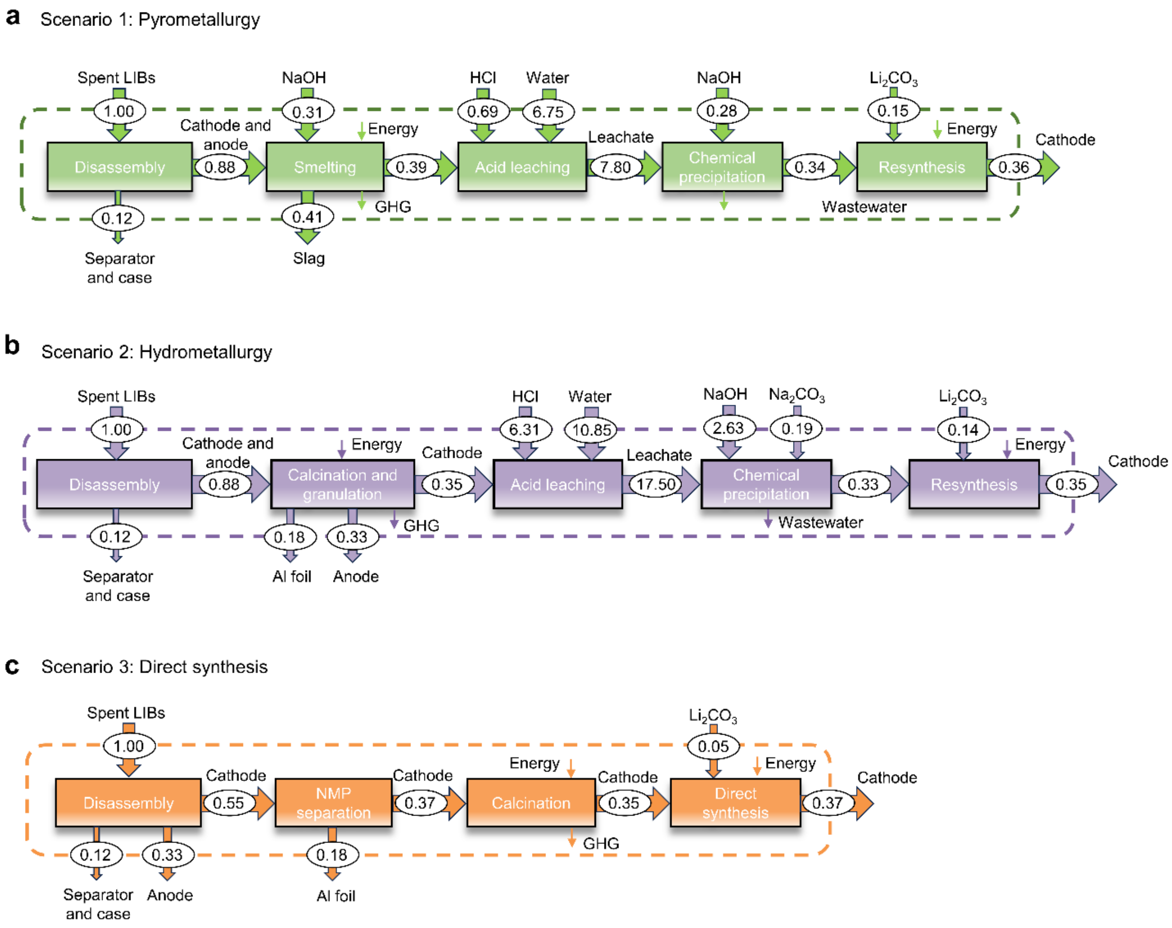

Fig. S52. Flow chart representation and boundary conditions for different LCA scenarios. (a) Scenario: Pyrometallurgy. (b) Scenario: Hydrometallurgy. (c) Scenario: Direct synthesis.

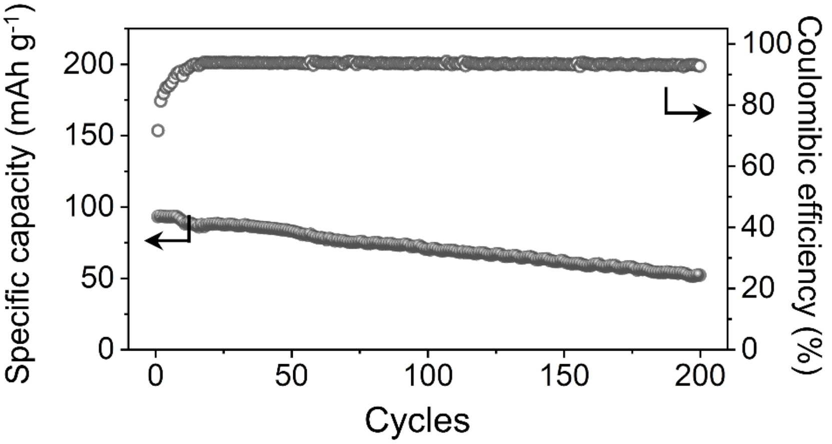

Fig. S53. Cycling performance of s-LCO at 0.2 C in the potential range of 3.0–4.2 V. The battery was cycled at 0.1 C for 10 cycles before operating at 0.2 C.

Table S1. Parameters for RER process*.

Precursors**	Doping content***	Mass (mg)	Current (A)	Time (s)	Mass after RER (mg)
s-LCO:Li_2CO_3	0	501	8	30	462
s-LCO:Li_2CO_3	0	500	12	30	451
s-LCO:Li_2CO_3	0	497	16	30	439
s-LCO:Li_2CO_3	0	500	25	30	423
s-LCO:Li_2CO_3	0	502	35	30	397
s-LCO:Li_2CO_3:MgO:Al_2O_3	MgO: 2 wt% Al_2O_3: 1 wt%	499	12	30	457
s-LCO:Li_2CO_3:MgO:Al_2O_3	MgO: 0.4 wt% Al_2O_3: 0.2 wt%	500	12	30	453
s-LCO:Li_2CO_3:MgO:Al_2O_3	MgO: 0.6 wt% Al_2O_3: 0.3 wt%	500	12	30	452
s-LCO:Li_2CO_3:MgO:Al_2O_3	MgO: 4 wt% Al_2O_3: 2 wt%	497	12	30	461
s-LCO:Li_2CO_3:MgO:Al_2O_3	MgO: 6 wt% Al_2O_3: 3 wt%	502	12	30	460
s-LCO:Li_2CO_3:MgO:Al_2O_3	MgO: 1 wt% Al_2O_3: 2 wt%	500	12	30	458
s-LCO:Li_2CO_3:$MgCO_3$:Al_2O_3	$MgCO_3$: 4 wt% Al_2O_3: 1 wt%	500	12	30	447
s-NMC:Li_2CO_3:MgO:Al_2O_3	MgO: 1 wt% Al_2O_3: 2 wt%	500	12	30	435
s-LCO:Li_2CO_3:MgO	MgO: 3wt%	500	12	30	459
s-LCO:Li_2CO_3:Al_2O_3	Al_2O_3: 3 wt%	501	12	30	455
s-LCO:Li_2CO_3:MgO:TiO_2	MgO: 2 wt% TiO_2: 1 wt%	500	12	30	454
s-LCO:Li_2CO_3:MgO:MnO_2	MgO: 2 wt% MnO_2: 1 wt%	498	12	30	446

Note: *RER, rapid electrothermal rejuvenation. **The content of Li_2CO_3 was kept at 15 wt%. ***The doping content here refers to the weight percentage of metal oxide added in the precursors, while 0 represents no dopants were added.

Table S2. Lattice parameters for r-LCO-MA under different temperatures.

Temperature (°C)	*a* (Å)	*b* (Å)	*c* (Å)	*V* (Å^3)
700	2.815	2.815	14.098	96.748

750	2.815	2.815	14.091	96.701
800	2.814	2.814	14.095	96.659
900	2.807	2.807	14.056	95.913
1000	2.796	2.796	13.837	93.680

Table S3. Lattice parameters for different LCO samples by XRD refinement results.

	a (Å)	*b* (Å)	*c* (Å)	*V* ($Å^3$)
c-LCO	2.814	2.814	14.046	96.323
s-LCO	2.813	2.813	14.179	97.192
r-LCO-MA	2.815	2.815	14.091	96.701

Table S4. Contents of Mg and Al dopants in the regenerated LCO after electrothermal treatment.

Sample	**Mg content (ppm)**	**Al content (ppm)**
r-LCO-MA0.6	2513 ± 231	1022 ± 156
r-LCO-MA1	4030 ± 529	1726 ± 467
r-LCO-MA3	12790 ± 477	5307 ± 1031
r-LCO-MA6	24910 ± 751	10731 ± 1404
r-LCO-MA9	37193 ± 1915	16280 ± 2120
r-LCO-M3	18920 ± 967	23.5 ± 1.8
r-LCO-A3	0.56 ± 0.08	16270 ± 1175

Note: *For r-LCO-MA sample, the initial input mass ratio of MgO/Al_2O_3 was set as 2:1 without specific mentioning.

Table S5. Materials flow for various scenarios.

Scenarios	**Pyrometallurgical method (kg)**	**Hydrometallurgical method (kg)**	**Direct recycling (kg)**	**RER (kg)**
NMP	0	0	0.185	0
12 M HCl	0.0345	0.316	0	0
NaOH	0.28	2.63	0	0
Na_2CO_3	0	0.19	0	0
MgO	0	0	0	0.007
Al_2O_3	0	0	0	0.0035

Li_2CO_3	0.15	0.14	0.05	0.05
Water	0.338	0.543	0	0
Discharging and collecting	1	1	1	1
Calcination and granulation	0	0.88	0	0
Separation	0	0	0.88	0.88
NMP washing	0	0	0.37	0
High-temperature smelting	0.88	0	0	0
Low-temperature calcination	0	0	0.37	0.37
Acid leaching	0.39	0.35	0	0
Chemical precipitation	7.80	17.50	0	0
Resynthesis	0.34	0.33	0	0
Direct regeneration	0	0	0.35	0
Electrothermal regeneration	0	0	0	0.35

Note: *The materials mass flow is normalized to process 1 kg of spent battery.

Table S6. Life cycle inventory.

Impact Category	Energy consumption (MJ)	GHG emission (kg)	Water consumption (kg)
NMP	89.58	5.55	3.51
12 M HCl	2.10	29.17	4.71
NaOH	31.96	2.32	12.54
Na_2CO_3	5.36	0.68	0.12
MgO	12.00	0.90	0.27
Al_2O_3	11.18	1.00	7.99
Li_2CO_3	121.98	12.05	44.92
Discharging and collecting	0.41	0.054	0.78
Calcination and granulation	0.21	0.33	0.53
Cathode separation	0.38	0.05	0.26
NMP washing	0.78	0.10	0.52
Smelting	2.24	1.40	1.51
Low-temperature calcination	0.20	0.53	0.14
Acid leaching for pyrometallurgical method	0.11	0.014	17.31
Acid leaching for hydrometallurgical method	0.11	0.014	30.99

Impact Category	Energy consumption (MJ)	GHG emission (kg)	Water consumption (kg)
Chemical precipitation	0.11	0.014	0.036
Resynthesis heating	18.84	2.95	12.63
Direct regeneration heating	7.05	1.01	4.73
Electrothermal heating	5.61	0.82	3.76

Note: *GHG, greenhouse gas. ** The environmental impacts or energy demands are normalized to process 1 kg of spent battery.

Table S7. Energy consumption for various scenarios.

Scenarios	Pyrometallurgical method (MJ)	Hydrometallurgical method (MJ)	Direct recycling (MJ)	RER(MJ)
NMP	0	0	16.57	0
12 M HCl	0.072	0.66	0	0
NaOH	8.95	84.05	0	0
Na_2CO_3	0	1.02	0	0
MgO	0	0	0	0.084
Al_2O_3	0	0	0	0.039
Li_2CO_3	18.30	17.08	6.10	6.10
SUM of Materials	27.32	102.81	22.67	6.22
Discharging and collecting	0.41	0.41	0.41	0.41
Calcination and granulation	0	0.18	0	0
Separation	0	0	0.33	0.33
NMP washing	0	0	0.29	0
High-temperature smelting	1.97	0	0	0
Low-temperature calcination	0	0	0.074	0.074
Acid leaching	0.043	0.039	0	0
Chemical precipitation	0.86	1.93	0	0
Resynthesis	6.41	6.22	0	0
Direct regeneration	0	0	2.47	0
Electrothermal regeneration	0	0	0	1.96
SUM of Process	9.69	8.78	3.57	2.78
SUM	37.0	111.6	26.3	9.0

Note: *The materials mass flow is normalized to process 1 kg of spent battery.

Table S8. GHG emissions for various scenarios.

Scenarios	Pyrometallurgical method (kg)	Hydrometallurgical method (kg)	Direct recycling (kg)	RER (kg)
NMP	0	0	1.03	0
12 M HCl	1.01	9.20	0	0
NaOH	0.65	6.09	0	0
Na_2CO_3	0	0.13	0	0
MgO	0	0	0	0.0063
Al_2O_3	0	0	0	0.0035
Li_2CO_3	1.81	1.69	0.60	0.60
SUM of Materials	3.46	17.11	1.63	0.61
Discharging and collecting	0.054	0.054	0.054	0.054
Calcination and granulation	0	0.29	0	0
Separation	0	0	0.044	0.044
NMP washing	0	0	0.037	0
High-temperature smelting	1.23	0	0	0
Low-temperature calcination	0	0	0.19	0.19
Acid leaching	0.0055	0.0049	0	0
Chemical precipitation	0.11	0.25	0	0
Resynthesis	1.00	0.97	0	0
Direct regeneration	0	0	0.35	0
Electrothermal regeneration	0	0	0	0.29
SUM of Process	2.40	1.57	0.68	0.58
SUM	5.9	18.7	2.3	1.2

Note: *The materials mass flow is normalized to process 1 kg of spent battery.

Table S9. Water consumption for various scenarios.

Scenarios	Pyrometallurgical method (kg)	Hydrometallurgical method (kg)	Direct recycling (kg)	RER (kg)
NMP	0	0	0.65	0
12 M HCl	0.16	1.49	0	0
NaOH	3.51	32.98	0	0
Na_2CO_3	0	0.022	0	0
MgO	0	0	0	0.0019

Al_2O_3	0	0	0	0.028
Li_2CO_3	6.74	6.29	2.25	2.25
Water	0.34	0.54	0	0
SUM of Materials	10.75	41.33	2.89	2.28
Discharging and collecting	0.78	0.78	0.78	0.78
Calcination and granulation	0	0.47	0	0
Separation	0	0	0.23	0.23
NMP washing	0	0	0.19	0
High-temperature smelting	1.33	0	0	0
Low-temperature calcination	0	0	0.052	0.052
Acid leaching	6.75	10.85	0	0
Chemical precipitation	0.28	0.63	0	0
Resynthesis	4.29	4.17	0	0
Direct regeneration	0	0	1.65	0
Electrothermal regeneration	0	0	0	1.31
SUM of Process	13.43	16.89	2.91	2.38
SUM	24.2	58.2	5.8	4.7

Note: *The materials mass flow is normalized to process 1 kg of spent battery.

Table S10. Materials and energy cost inventory.

Scenarios	Materials cost ($)	Energy cost ($)
NMP	2800	0
12 M HCl	179	0
NaOH	1315	0
Na_2CO_3	284	0
MgO	425	0
Al_2O_3	540	0
Li_2CO_3	15490	0
Water	1.085	0
Discharging and collecting	0	7.33
Calcination and granulation	0	3.76
Separation	0	6.80
NMP washing	0	13.95

High-temperature smelting	0	40.07
Low-temperature calcination	0	3.58
Acid leaching	0	1.97
Chemical precipitation	0	1.97
Resynthesis	0	337.03
Direct regeneration	0	126.12
Electrothermal regeneration	0	100.29

Note: *The materials mass flow is normalized to process 1 tonne of spent battery. **The consumed energy is assumed to be from electricity, and the industrial price of electrical energy in Texas, USA, is \$0.0644 kWh[27].

Table S11. Cost evaluation of various scenarios.

Scenarios	Pyrometallurgical method (\$)	Hydrometallurgical method (\$)	Direct recycling (\$)	RER (\$)
NMP	0	0	518.00	0
12 M HCl	6.18	56.47	0	0
NaOH	368.20	3458.45	0	0
Na_2CO_3	0	53.96	0	0
MgO	0	0	0	2.98
Al_2O_3	0	0	0	1.89
Li_2CO_3	2323.50	2168.60	774.50	774.50
Water	0.37	0.59	0	0
SUM of Materials	2698.24	5738.07	1292.50	779.37
Discharging and collecting	7.33	7.33	7.33	7.33
Calcination and granulation	0	3.31	0	0
Separation	0	0	5.98	5.98
NMP washing	0	0	5.16	0
High-temperature smelting	35.26	0	0	0
Low-temperature calcination	0	0	1.32	1.32
Acid leaching	0.77	0.69	0	0
Chemical precipitation	15.35	34.44	0	0
Resynthesis	114.59	111.22	0	0
Direct regeneration	0	0	44.14	0
Electrothermal regeneration	0	0	0	35.10
SUM of Process	173.30	156.98	63.94	49.74

Grinder	4.4	4.4	0	0
Scraper	0	0	13.2	13.2
Agitator	157.5	702	33.3	0
Filter	78	175	37	0
Low-temperature furnace	40.88	40.88	17	17
High-temperature furnace	48.51	46.53	39.6	0
Arc welder	0	0	0	6.5
Capital Cost	426.29	871.81	140.10	36.70
Total Cost	**3297.8**	**6766.9**	**1496.5**	**865.8**

Note: *The materials mass flow is normalized to process 1 tonne of spent battery.

Table S12. Calculated profit of various scenarios.

Scenarios	**Pyrometallurgical method ($)**	**Hydrometallurgical method ($)**	**Direct recycling ($)**	**RER ($)**
Cost	3297.8	6766.9	1496.5	865.8
Other expense	3980	3980	3980	3980
Income	20610.0	20037.5	21182.5	23655.0
Profit	13332	9291	15706	18809

Note: *The materials mass flow is normalized to process 1 tonne of spent battery. **Other expense includes direct labor ($150 tonne^{-1}), depreciation ($1960 tonne^{-1}), variable overhead ($450 tonne^{-1}), sales and administration ($640 tonne^{-1}), research and development ($780 tonne^{-1}), which are calculated from the EverBatt2020 database.

References

1. S. L. Dudarev, G. A. Botton, S. Y. Savrasov, C. Humphreys, A. P. Sutton. *Phys. Rev. B* **1998**, *57*, 1505.
2. G. Kresse, J. Furthmuller. *Phys. Rev. B* **1996**, *54*, 11169-11186.
3. P. E. Blöchl. *Phys. Rev. B* **1994**, *50*, 17953.
4. J. P. Perdew, K. Burke, M. Ernzerhof. *Phys. Rev. Lett.* **1996**, *77*, 3865-3868.
5. H. J. Monkhorst, J. D. Pack. *Phys. Rev. B* **1976**, *13*, 5188.
6. R. Sharpe, R. A. House, M. J. Clarke, D. Förstermann, J.-J. Marie, G. Cibin, K.-J. Zhou, H. Y. Playford, P. G. Bruce, M. S. Islam. *J. Am. Chem. Soc.* **2020**, *142*, 21799-21809.
7. J. Heyd, G. E. Scuseria, M. Ernzerhof. *J. Chem. Phys.* **2003**, *118*, 8207-8215.
8. D. K. Roper, W. Ahn, M. Hoepfner. *J. Phys. Chem. C* **2007**, *111*, 3636-3641.

9. Y. Cheng, S. Cheng, B. Chen, J. Jiang, C. Tu, W. Li, Y. Yang, K. Huang, K. Wang, H. Yuan, J. Li, Y. Qi, Z. Liu. *J. Am. Chem. Soc.* **2022**, *144*, 15562-15568.

10. W. Chen, R. V. Salvatierra, J. T. Li, C. Kittrell, J. L. Beckham, K. M. Wyss, N. La, P. E. Savas, C. Ge, P. A. Advincula, P. Scotland, L. Eddy, B. Deng, Z. Yuan, J. M. Tour. *Adv. Mater.* **2023**, *35*, e2207303.

11. Y. Cheng, J. Chen, B. Deng, W. Chen, K. J. Silva, L. Eddy, G. Wu, Y. Chen, B. Li, C. Kittrell, S. Xu, T. Si, A. A. Martí, B. I. Yakobson, Y. Zhao and J. M. Tour, *Nat. Sustain.*, 2024, **7**, 452-462.

12. ISO, 2006. Life cycle assessment-requirements and guidelines (ISO 14044:2006).

13. N. Li, J. Guo, Z. Chang, H. Dang, X. Zhao, S. Ali, W. Li, H. Zhou, C. Sun. *RSC Adv.* **2019**, *9*, 23908-23915.

14. M. Wang, A. Elgowainy, U. Lee, A. Bafana, S. Banerjee, P. T. Benavides, P. Bobba, A. Burnham, H. Cai, U. R. Gracida-Alvarez. Summary of Expansions and Updates in GREET® 2021. (Argonne National Lab.(ANL), Argonne, IL (United States), 2021).

15. Q. Dai, J. Spangenberger, S. Ahmed, L. Gaines, J. C. Kelly, M. Wang. EverBatt: A closed-loop battery recycling cost and environmental impacts model. (Argonne National Lab.(ANL), Argonne, IL (United States), 2019).

16. J. Wang, K. Jia, J. Ma, Z. Liang, Z. Zhuang, Y. Zhao, B. Li, G. Zhou, H.-M. Cheng. *Nat. Sustain.* **2023**, *6*, 797-805.

17. https://greet.es.anl.gov/, accessed May 15th, 2024.

18. https://www.anl.gov/amd/everbatt, accessed May 15th, 2024.

19. https://www.cityofbryan.net/commercialindustrial-metering-rates/, accessed May 15th, 2024.

20. https://www.industryarc.com/report/16180/n-mmethyl-2-pyrrolidone-market.html, accessed May 15th, 2024.

21. https://www.chemanalyst.com/pricing-data/hydrochloric-acid-61, accessed May 15th, 2024.

22. https://www.aranca.com/knowledge-library/articles/business-research/price-corrections-in-global-caustic-soda-market, accessed May 15th, 2024.

23. https://medium.com/intratec-products-blog/sodium-carbonate-prices-latest-historical-data-in-several-countries-8d36c8e3b8f1, accessed May 15th, 2024.

24. https://www.chemanalyst.com/pricing-data/magnesium-powder-1513, accessed May 15th, 2024.

25. https://www.intratec.us/chemical-markets/aluminum-oxide-price, accessed May 15th, 2024.

26. https://tradingeconomics.com/commodity/lithium, accessed May 15th, 2024.

27. https://www.eia.gov/electricity/monthly/epm_table_grapher.php?t=epmt_5_6_a, accessed May 15th, 2024.

28. https://www.alibaba.com/product-detail/220v-380v-high-professional-stainless-steel_1600116824048.html, accessed May 15th, 2024.

29. https://www.alibaba.com/product-detail/new-style-manual-grinding-and-scraping_1601038516727.html, accessed May 15th, 2024.

30. https://www.alibaba.com/product-detail/agitator-mixer-stainless-steel-tank-mixer_60616253974.html?s=p, accessed May 15th, 2024.

31. https://www.alibaba.com/product-detail/1000l-h-uf-water-treatment-system_60766650935.html, accessed May 15th, 2024.

32. https://www.amazon.com/dekopro-machine-digital-display-electrode/dp/b07nwfb2s9/ref=sr_1_8?th=1, May 15th, 2024.

33. https://hq.smm.cn/, access May 15th, 2024.

34. D. X. Luong, K. V. Bets, W. A. Algozeeb, M. G. Stanford, C. Kittrell, W. Chen, R. V. Salvatierra, M. Ren, E. A. McHugh, P. A. Advincula, Z. Wang, M. Bhatt, H. Guo, V. Mancevski, R. Shahsavari, B. I. Yakobson, J. M. Tour. *Nature* **2020**, *577*, 647-651.

35. J.-N. Zhang, Q. Li, C. Ouyang, X. Yu, M. Ge, X. Huang, E. Hu, C. Ma, S. Li, R. Xiao. *Nat. Energy* **2019**, *4*, 594-603.

36. E. Fan, J. Lin, X. Zhang, R. Chen, F. Wu, L. Li. *Small Methods* **2021**, *5*, 2100672.

37. Z. Fei, Y. Zhang, Q. Meng, P. Dong, J. Fei, S. Zhou, K. Kwon. *ACS Sustain. Chem. Eng.* **2021**, *9*, 11194-11203.

38. S. Zhou, Z. Fei, Q. Meng, P. Dong, Y. Zhang, M. Zhang. *ACS Appl. Energy Mater.* **2021**, *4*, 12677-12687.

39. N. Zhang, W. Deng, Z. Xu, X. Wang. *Carbon Energy* **2023**, *5*, e231.

40. W. Kong, J. Zhang, D. Wong, W. Yang, J. Yang, C. Schulz, X. Liu. *Angew. Chem. Int. Ed.* **2021**, *133*, 27308-27318.

41. Y. Huang, Y. Zhu, H. Fu, M. Ou, C. Hu, S. Yu, Z. Hu, C. T. Chen, G. Jiang, H. Gu, H. Lin, W. Luo, Y. Huang. *Angew. Chem. Int. Ed.* **2021**, *60*, 4682-4688.

42. Z. Wang, Z. Wang, H. Guo, W. Peng, X. Li, G. Yan, J. Wang. *J. Alloys Compd.* **2015**, *621*, 212-219.

43. J.-H. Shim, N.-H. Cho, S. Lee. *Electrochim. Acta* **2017**, *243*, 162-169.

44. M. Yoon, Y. Dong, Y. Yoo, S. Myeong, J. Hwang, J. Kim, S.-H. Choi, J. Sung, S. J. Kang, J. Li, J. Cho. *Adv. Funct. Mater.* **2020**, *30*, 1907903.

45. Q.-A. Huang, Y. Shen, Y. Huang, L. Zhang, J. Zhang. *Electrochim. Acta* **2016**, *219*, 751-765.